The neural mechanisms of fast versus slow decision-making

Mostafa Nashaat[1†*], Hatem Oraby[1†], Flutra Krasniqi[1], Sek Teng Goh-Sauerbier[1], Marion Bosc[2,3], Sandra Koerner[1], Sedef Karayel[4], Adam Kepecs[5], Matthew E. Larkum[1*]

[1]Institute for Biology, Humboldt University of Berlin, D-10117 Berlin, Germany

[2]Cold Spring Harbor Laboratory, Cold Spring Harbor, NY 11724, USA

[3]Neural circuits and immunity in psychosis laboratory, The Francis Crick Institute, London NW1 1AT, UK

[4]Charité – Universitätsmedizin Berlin, Einstein Center for Neurosciences Berlin, 10117, Berlin, Germany.

[5]Department of Neuroscience and Department of Psychiatry, Washington University in St. Louis, St. Louis, MO 63110, USA

[†]These authors contributed equally

*Corresponding authors: Matthew Larkum (matthew.larkum@hu-berlin.de), Mostafa Nashaat (mostafa.abdelhamid@hu-berlin.de)

Summary

Not all decisions are created equal; factors such as the difficulties or associated costs affect the time spent to make decisions. This is variously interpreted as speed/accuracy, fast/slow, or impulsivity/deliberateness tradeoffs according to different models of behaviour[1–5]. Regardless, it is generally assumed that decision latency reflects the neural mechanisms underlying behavioural strategy and cognitive investment. However, such investigations have been difficult in mice which are consistently impulsive. Here, we show that manipulating cost, using a novel floating-platform paradigm, overcomes the natural impulsivity of mice, more closely matching human behaviour. Furthermore, this approach allowed us simultaneously to measure the flow of activity from medial to lateral frontal cortex (MFC→LFC) and record sequences of single neuron activity with 2-photon imaging. Surprisingly, MFC display a different mode of operation, with high vulnerability to optical inhibition compared to LFC. Furthermore, the balance in choice coding at the beginning of sequences in MFC correlated with trial history and behavioural strategy. We found that for optimal performance, slow sequences in MFC showed declining numbers of active neurons whereas the opposite was true in LFC. Our results suggest that while LFC acts as an integrative motor threshold, MFC plays a larger cognitive role in the selection and timing of decisions than previously thought. Our study offers a methodological and mechanistic framework in mouse frontal cortex to understand the neural basis of voluntary decision making.

Results

In natural decision-making paradigms used in humans there are many variables at play such as task history (priors), task difficulty (evidence), stakes (cost/reward) and attention [3,4,6,7]. The causal neural mechanisms influencing behaviour are best studied in head-fixed mice. However, contrary to humans, mice tend to exhibit impulsive behaviour exclusively under most commonly used approaches that influence the natural volition of the mice to make decisions, i.e. free time to sample (Fig. 1a)[8–11]. In this study, we utilize head-fixed mouse preparation combined with air floating nose-poke platform technology[12], enabling the use of advanced neural acquisition and perturbation techniques, while simultaneously facilitating more natural, quasi-freely-moving behaviour[13,14]. We call our system floating platform (Figure 1b; Extended Fig. 1a). Head-fixed mice voluntarily navigate a nose-poke floating environment to perform a two-alternative forced choices visual discrimination task with unconstrained sampling times (Fig. 1c; Extended Fig. 1b; “free sampling time”). Like several studies on humans, we adapted the classical Random Dots Kinematogram (RDK) free sampling paradigm (Fig. 1d)[10,15,16]. Mice discriminate the direction of moving dots to execute a motor movement congruent with the majority of moving dots’ direction to collect reward (Supplementary Video 1). Stimulus saliency is determined by varying the dots’ coherence so that the percentage of the dots moving toward the reward direction determines the trial difficulty (Extended Fig. 1b, c; Supplementary Video 2). By controlling airflow underneath the floating platform, we manipulated the effort, decision cost, required

by head-fixed mice to move the platform which impacted decisions' time and accuracy (Extended Fig. 2)[17].

In humans, the optimal strategy to perform the RDK task is to vary sampling time based on dot coherence, where subjects spend more time in low coherence compared to high coherence[18]. We compared the decision accuracy and sampling time of both human and mice across different coherences during RDK task (Fig. 1d,f; example human subject with 797 trials and mouse subject with 3519 trials). Although humans performed slightly better than mice (presumably due to their higher visual acuity for motion detection), both mice and humans adopted very similar strategies, voluntarily increasing their sampling time in difficult trials (Fig. 1e, f). Using this voluntary-sampling paradigm, sampling times varied from trial to trial across single sessions (Fig. 1g; 0.3-3.0 s, average 0.8±0.5 s; n=1, session=15, trials=3,519 trials), and could be divided into three categories, reflecting fast ("impulsive", 1st third), typical ("normal", 2nd third) and slow ("deliberate", last third) behaviour (Fig. 1g). This variability in sampling time is reflected in the decision accuracy for different difficulties (Fig. 1h). We found that impulsive behaviour in rodents is similar to humans under competition policy aiming at maximizing the number of correct outcomes (Extended Fig. 3a; human accuracy competition, n=34, trials=12,631; human maximum correct-outcome competition n=22, trials=20,940; mice floating platform n=20, trials=63,904). In both, a speed-accuracy trade-off is noticeable in which errors are significantly correlated with fast sampling time (Extended Fig. 3b, c)[19]. Here, regardless of difficulty, slow (deliberate) decisions exhibited significantly higher performance levels than fast (impulsive) decisions (Extended Fig. 3d for an example mouse in Fig. 1g; see also Extended Fig. 3e for all mice), whereas fast (impulsive) decisions had a higher tendency to be erroneous regardless of difficulty (Fig. 1i; error (red)=682 trials; correct (green)=2,834 trials).

Frontal calcium wave mediates decision-making strategy.

To investigate the cellular mechanisms of fast versus slow decisions, we exploited the floating platform approach in combination with widefield imaging and optogenetic perturbation of specific cortical regions (Fig. 2a; and Extended Fig. 4a). For widefield calcium imaging, we used a transgenic mouse line (Thy1 GP4.3) to express a genetically encoded calcium indicator (GCAMP6s) in cortical excitatory neurons, while mice performed the RDK task using the voluntary-sampling paradigm (free sampling; Fig. 1c)[20]. Given the variable nature and timing of behavioural strategies (Fig. 1g, and Extended Fig. 3b), we decided to first focus on typical behavioural trials (sampling times of 1.0-1.2s; Extended Fig. 4c) while using widefield imaging to characterize activity around the cortex (Fig. 2b, c and Extended Fig. 4c, d)[21]. We observed that all areas around the cortex were active at some time during the sampling with a distinct spatio-temporal pattern originating from the medial axis of dorsal neocortex at the start of sampling (Fig. 2b, left) traversing radially until the animal made a decision (Fig. 2b and Extended Fig. 4e, decision made after last panel, i.e. 1.0-1.2s).

To identify the contribution of the different cortical areas, we used a selective optogenetic perturbation approach in behaving head-fixed mice expressing genetically encoded ChR2 in all inhibitory neurons of mouse neocortex (VGAT-cre/ChR2; Fig. 2d , top left)[22]. Since the time of the animal's movement (i.e. the decision) was not fixed in the free-sampling paradigm, it was necessary to use a fixed-time paradigm to restrict the optogenetic inhibition to sampling and not overlap with motor initiation (Extended Fig. 5a). Using bilateral targeting of different cortical areas, we optogenetically inhibited different cortical regions during 1s fixed sampling time (Figure 2d, left panel; V1, n=16 sessions from 7 mice; PPC, n=12 sessions from 6 mice; RSP, n=9 sessions from 3 mice; MFC, n=17 sessions from 7 mice; LFC, n=21 sessions from 7 mice)[23]. While optogenetic silencing caused significant drops in performance across most cortical regions, the highest drop in performance was observed in MFC (28.53% ±3.79% SEM) and LFC (26.25% ±4.03% SEM) (Fig 2d right panel; Extended Fig. 5b-g; two-tailed paired t-test)[23]. These data suggested that the calcium wave trajectory through MFC and LFC is required for optimal decision-making[24].

To investigate this further, we focused on the flow of activity in the medial-lateral axis of frontal cortex using the free-sampling paradigm (Fig. 2e, right panel; MFC→LFC). We examined the dynamics of the frontal calcium wave during the different decision-making strategies, i.e. fast (impulsive, 0-0.33 quantile), typical (normal, 0.33-0.66), and slow (deliberate, 0.66-1 quantile; Fig. 2f, n=6 mice, 18 sessions). Here, we saw a clear distinction between fast and slow strategies; whereas slow decision-making closely resembled typical trials, activity in the two frontal regions was quite dissimilar. During typical and slow strategies fluorescence activity in MFC was antipodal (mirror-image) to activity in LFC (Extended Fig. 6a, n=6 mice, 18 sessions), even though both regions contributed equally to performance (Fig. 2d). Interestingly, while LFC was active before the decision, MFC was at its lowest point (Fig. 2e). However, during fast strategy, activity levels in MFC and LFC were truncated and no longer antipodal, resembling "aborted" trials (Extended Fig. 6b). As mice sample the stimulus, the antipodal nature of calcium wave dynamics at the end of sampling reflected behavioural strategy (Extended Fig. 6c-f; Δ fast=0.39 ±0.06, Δ typical=0.66 ±0.05, Δ slow=0.73 ±0.04)

Single-cell activity during fast and slow behaviour

These data imply that activity in MFC at the beginning of the sampling period contributes more to the eventual decision, whereas the crucial activity in LFC is at the end of the sampling period. To test this hypothesis, we used optogenetic inhibition in both regions (Fig. 3a). Firstly, since the timing of inhibition was crucial, it was necessary to use fixed sampling in order to precisely block either the first (0-0.35 s) or last third (0.65-1.0 s) of sampling (Fig. 3b)[25]. We also repeated the widefield imaging experiments using the fixed sampling (1s) (i.e. typical) and observed similar calcium wave dynamics in cortex (Fig. 3b and Extended Fig. 7a, b). As expected, optogenetic inhibition in the first third of sampling had a bigger effect when applied to MFC (n=7, sessions=19,16.31% ±2.38% SEM) than LFC (n=10, sessions=19, 8.79% ±2.56% SEM) (Fig. 3c and Extended Fig. 7c-e; Early

inhibition). However surprisingly, optogenetic inhibition at the end of sampling of both MFC (n=7, sessions=20, 15.18% ±3.20% SEM) and LFC (n=9, sessions=22, 14.37% ±3.37% SEM) had a similar and large effect on performance (Fig. 3c and Extended Fig. 7c-e; Late inhibition), implying that optimal decision-making requires decreased activity in MFC.

The surprising effectiveness of MFC at the end of sampling suggests some complexity to the remaining activity that might be addressed at the single-cell level. Since the floating platform approach allows head-fixed nose-poke behaviour, it was possible to carry out fluorescence calcium imaging on single neurons directly using two-photon microscopy in both MFC (n=4; s=10) and LFC (n=4; s=11) during behaviour (Figure 3d; see Methods). Single L2/3 pyramidal neurons exhibited distinct calcium responses during different decision strategies (Figure 3e). Therefore, the average activity of each neuron was normalized for all trials for each decision-making strategy and used to construct heat maps (Fig. 3f). Most neurons exhibited maximum firing in a stereotypical temporal window during sampling. Plotting neurons chronologically based on their mean maximum firing across each decision strategy suggested temporal sequences of peak firing that were consistent on average across trials (Fig. 3g)[26–28]. Despite the differences in sampling duration, these temporal sequences were even maintained across behavioural strategies (i.e. fast versus slow; Extended Fig. 8a, b; see Methods).

More MFC neurons fired at an early stage of sampling while LFC neurons were more tuned to the end of sampling and movement epochs[29]. Additionally, MFC neurons showed a tendency to fire more persistently around their peak firing than neurons in LFC (Extended Fig. 8c-g). Neurons in MFC showed a tendency towards sparse but reliably firing immediately prior to the decision. Combined with the influence of optical inhibition on MFC, this implies a refinement (rather than simply decay) of neuronal firing. Computing the combined average across all cells (Extended Fig. 9a), yielded comparable dynamics to widefield imaging responses (Extended Fig. 9b, c; cf. 2e & 3b). In conclusion, optogenetic inhibition and 2-photon imaging revealed that the neural mechanisms underlying optimal decision-making involve both sparse neural activity in MFC and increasing neuronal engagement in the LFC.

Two modes of operation in MFC versus LFC

The data so far raise the hypothesis that MFC and LFC have different modes of operation, such as a causal neuronal chain reaction (i.e. sequence-dependent) or sequence-independent continuous sensory integration. To investigate this, we reasoned that disrupting the sequence in the middle would impact the timing and performance differently to continuous integration (Fig. 3h, top)[30]. Here, we chose to inhibit during a free-sampling paradigm (between 0.3 to 0.9 seconds when decisions were most commonly made), to accentuate the impact of disturbing the sequence on behaviour (Fig. 3, bottom ‘grey trace’). We found that LFC inhibition caused small, divergent effects on sampling time distribution, either slightly speeding up or slowing down motor initiation, leading to small

changes in peak sampling. ('magenta trace' in example mouse in Fig. 3H, bottom; n=8, sessions=24; Fig. 3i, left; 3 out of 8 mice showed early shift in mode=0.15ms ±0.05 SEM, while 5 of 8 mice showed delayed shift in mode=0.41ms ±0.06 SEM; Extended Fig. 10a). Meanwhile, mice performance deteriorated during LFC inhibition but recovered to similar values of control performance after the end of the inhibition (Fig. 4i, right and Extended Fig. 10b, c). On the other hand, MFC inhibition led to consistent much longer delays in the peak sampling time ('blue trace' in example mouse in Fig. 3H, bottom; n=8, sessions=27; Fig. 3i, left; all mice showed delayed shift in mode=0.750ms ±0.09 SEM, Extended Fig. 10a) that resembled a "shift" in the distribution of sampling with a sustained drop in performance after the end of inhibition (Fig. 4i, right and Extended Fig. 10c). The effect of MFC inhibition during free-sampling emphasizes its central role in tuning sampling time and performance (Extended Fig. d-f). These results are consistent with the hypothesis that making a decision engages MFC in a sequence-dependent refinement process, versus a sequence independent integrative process in LFC.

To investigate this further, we examined the 2-photon single-neuron responses based on the animal's choice (left versus right; Fig. 4a, left). Interestingly, the heat maps consisting of only trials where the animal chose to go left or right, showed similar sequences (Fig. 4b, top). Nevertheless, we could identify a subset of neurons to be choice-selective (Fig. 4d, bottom), when the peak mean activity during sampling was significantly higher for one choice direction (green, "animal's choice-matched") versus the other (brown, "animal's choice-mismatched"). Using this definition, neurons fell into two categories; tuned (either left or right) or non-selective. We observed a higher percentage of choice-encoding neurons in LFC versus MFC across all behavioural strategies (Fig, 4c; 33.07 ±3.82%SEM versus 18 ±-3%SEM; Fig. 4c). The peak activity of choice-selective neurons occurred at different times across the whole period of sampling (Fig. 4d, top). However, interestingly, we found that selectively could vary as a function of behavioural strategy even within a single neuron (Fig. 4e). We therefore asked whether the evolution of choice-selectivity across different behavioural strategies reflected the mode of operation of MFC versus LFC (Fig. 4f, top). To quantify this, we binned neurons according to their temporal peak activity comparing matched versus mismatched responses for each bin (Fig. d, middle panel, fast and bottom panel, slow); Extended Fig.11a, b). To clarify this concept, we used the metaphor of a balance (Extended Fig. 11a, b) to encapsulate the evolution of choice-balance, where the number of the balls on each side represents the "weight of activity" across matched and mismatched trials. For comparison, we also overlaid the average population 2-photon activity from all L2/3 neurons (dotted lines; cf. Extended Fig. 9g) on the choice-selectivity histograms.

Using choice-balance as a metric, we conclude that slow behaviour commences from a more balanced initial state, a trend consistent in both MFC and LFC. In contrast, fast behaviour is characterized by an initial state of imbalance in matched versus mismatched activity. In addition, a consistent observation across all conditions was the emergence of an imbalance in choice-activity by the end of the sampling period. However, MFC and LFC reached this imbalance via different mechanisms. In particular, during optimal

strategy, slow behaviour, MFC started with a high level of activity, which was refined over the sampling period, primarily through the reduction (or refinement) of mismatched activity rather than matched activity. In general, the results can therefore also be interpreted in terms of another metric we refer to as “coding efficiency” (matched – mismatched / matched), where efficiency is the propensity to choose the matched direction at a given time (Fig. 4f, left). This metric allowed us to describe the transformation of activity in terms of its influence on the choice taken. We found that coding efficiency highly increased over sampling for slow behaviour, whereas it decreased for fast behaviour (Fig 4f, left and Extended Fig. 11c). Finally, the timepoint for the decision (i.e. termination of sampling) correlated with a threshold value of matched activity in LFC (Fig. 4g).

Our investigation confirms the hypothesis of two distinct operational modes in the MFC and LFC, albeit in a complex and nuanced manner. We observed that both regions exhibit increased coding efficiency during slow decisions and a decrease in efficiency during fast decisions. However, this similarity belies underlying differences: the MFC's increase in efficiency is linked to a reduction in overall activity coupled with refined choice-selectivity, whereas the LFC achieves this through heightened overall activity and a thresholding operational mode. These findings not only validate our hypothesis of differing MFC and LFC functions but also reveal the intricate mechanisms underpinning their roles in voluntary decision-making processes.

Influence of current evidence versus prior experience on behavioural strategy

Up to this point, we have shown that activity selective for the eventual choice builds up over sampling. Since optogenetic inhibition of MFC and LFC at the end of sampling (i.e. the last neurons in the sequence) disrupts performance, this suggests that the sequences of firing in both areas combine to produce an output that instructs another brain area (e.g. M1) to carry out a decision-based motor action. In other words, this activity represents the end of a “computation” or function (i.e. choice = $f(x,y,...)$, where x (such as priors i.e. trial history), y (such as evidence i.e. motion coherence), etc., are types of information, decision-relevant variables, available to the animal[31,32].

During fast behavioural strategy, the animal initiates the trial with high choice coding efficiency in both MFC and LFC (Fig. 4f). This raises the question as to why, under these circumstances, the animals are already having a clear choice preference before sampling, i.e. what other decision-relevant variable(s) influenced the animals’ choice? Firstly, we found that mice (like humans) tend to be cautious ‘slow’ after incorrect trials (post error slowing ‘PES’; Fig. 5a and Extended Fig. 12a, b)[33,34]. During fast decisions, mice exhibited high rate of both repeating previous correct choices (Win/stay) and averting from previous incorrect choices (lose/switch; extended Figure 12c, d). This is consistent with prior outcome as a decision-relevant variable affecting coding efficiency at the beginning of a trial. As we showed earlier (Figs. 2&3), activity in MFC tended to be higher than in LFC at the beginning of sampling (Fig. 5b, LHS, grey area). Furthermore, optogenetic inhibition at the start of sampling affected performance significantly more

when applied to MFC than LFC (Fig. 3c). Likewise, performance and sampling duration was affected more by mid-sequence inhibition (Fig. 3h&i). This implies that MFC (not LFC) plays a central role in tuning behavioural strategy during the early phase of sampling. We therefore examined more closely the neural activity at the start of sampling in both MFC and LFC (±100 ms; Fig. 5b). Consistent with our previous findings, we found that the activity level in MFC at the start of sampling significantly correlated with sampling duration and performance (Fig. 5b, RHS; MFC r=0.343 - p=0.011 – Slope=0.037, and LFC r=0.069 - p=0.662 – Slope=0.007; Extended Fig. 13a). These findings suggest that an initial state modulation in MFC plays a significant role in mediating behavioral strategy[35]. Therefore, we conclude that decision-relevant variables at the beginning of sampling, such as previous trial outcome, must influence performance and sampling duration predominantly via MFC.

To investigate the influence of trial history at the start of sampling in MFC, we examined neural responses to previous choice direction and outcome in the way they influence animal's choice (Fig. 5c). We found that the outcome of the previous trial significantly influenced the balance of match-to-mismatch activity of both previous and current choice-direction, consequently affecting sampling duration (Fig. 5d, and Extended Fig. 13b, c). MFC imbalanced neural representation after correct choice may resembles a history dependent update of an accumulator's starting point that drives fast (impulsive) behaviour (Extended Fig. 14a)[32,36,37]. Consistently, we found neural activity in the MFC (not LFC) selective for previous outcome significantly discriminative to behavioural strategy. In our case, mice optimize, update, their sampling strategy on a trial-by-trial basis according to previous trial evidence and outcome (Extended Fig. 14c, d).

In this behavioural paradigm, we assume a major decision-relevant variable is the direction of the moving dots and their coherence, i.e. the "evidence". Did the animals use the extra time during slow behaviour to more closely evaluate the evidence? Here, we found that the effect of stimulus difficulty on sampling time (i.e. the slope of sampling time versus coherence), was much greater during slow behaviour (Fig 5e, fast strategy slope= 0.02, θ=1.22°; slow strategy slope=0.10, θ=5.66°). We therefore revisited the way coding efficiency evolved over sampling (i.e. coding efficiency at the start - end of sampling) as a function of difficulty (Fig. 5f, and Extended Fig. 15). Here, a positive change in coding efficiency presumably reflects higher engagement of frontal cortex for determining the direction of choice. We found mostly positive coding efficiencies during slow behaviour versus negative values during fast behaviour (Fig. 15). Note: the negative value during fast behaviour reflects the already high coding efficiency at the start of sampling (due to priors). Lastly, we compared stimulus-tuned neurons with previous choice-tuned neurons (Extended Fig.16). Interestingly, we found both evidence-selective neurons that exhibited higher activity for easy stimuli as well as for hard stimuli, as well as neurons that encoded only trial difficulty but not choice per se (MFC=5.76 ±1.07 SEM and LFC=7.85 ±1.69 SEM)[38]. Overall, we found more prior-tuned neurons during fast behaviour and more evidence-tuned neurons during slow behaviour (Extended Fig.16)[39].

In conclusion, we have shown that both MFC and LFC contribute to decision-making but with distinctively different modes of operation (Fig. 5g, 5h). Surprising, we found that MFC contributed to the eventual choice at all time points whereas LFC contributed most towards the end of sampling. We show neural evidence that a threshold level of activity in LFC determines the time of decision. The single-cell (2P) data revealed that neurons tend to fire in distinct temporal windows in stereotypical sequences (rather than via persistent activity over sampling). In MFC, slow decisions are characterized by a refinement mode, involving neural activity representing all options at the beginning of sampling ("proposed choices") that are refined down to a small but homogenous population by the time of decision. This sparse neuronal activity nevertheless contributed equally to the eventual choice of the animal with high coding efficiency. As fast choices exhibit high correlation with trial history effect, MFC initial state seems to be locked. After correct trials, MFC activity showed selective inhibition of neural activity representing one of the two choices, reflecting a history dependent update at start of sampling[40]. Despite lack of consensus on the homology between mouse and primate frontal cortices, MFC, also known as medial M2, has anatomical and functional properties very similar to subdivisions of medial prefrontal cortex in primates[23,41,42]. Accordingly, our findings shed light on the primary role of MFC on behavioural flexibility and voluntary movement similar to its counterparts in primates[43–45]. Previous work has shown that MFC operates under the influence of other brain regions (i.e. striatum, parietal cortices) suggesting potential sources for modulating MFC initial state during different behavioural strategies[46–50]. Our results suggest that the interaction between the medial and lateral frontal cortices during voluntary decision-making involves a complex balance of neural activity across these regions. This interplay underpins the cognitive shift from fast to slow, thereby enhancing our understanding of the neural foundations of decision-making.

References

1. Kahneman, D. *Thinking, Fast and Slow*. 499 (Farrar, Straus and Giroux, New York, NY, US, 2011).
2. Luce, D. Response Times: Their Role in Inferring Elementary Mental Organization. in (1986).
3. Gold, J. I. & Shadlen, M. N. The Neural Basis of Decision Making. *Annual Review of Neuroscience* **30**, 535–574 (2007).
4. Bogacz, R., Brown, E., Moehlis, J., Holmes, P. & Cohen, J. D. The physics of optimal decision making: A formal analysis of models of performance in two-alternative forced-choice tasks. *Psychological Review* **113**, 700–765 (2006).
5. Ratcliff, R. & McKoon, G. The Diffusion Decision Model: Theory and Data for Two-Choice Decision Tasks. *Neural Comput* **20**, 873–922 (2008).
6. Glimcher, P. W. The Neurobiology of Visual-Saccadic Decision Making. *Annual Review of Neuroscience* **26**, 133–179 (2003).
7. Kepecs, A., Uchida, N., Zariwala, H. A. & Mainen, Z. F. Neural correlates, computation and behavioural impact of decision confidence. *Nature* **455**, 227–231 (2008).
8. Schwarz, C. *et al.* The head-fixed behaving rat—Procedures and pitfalls. *Somatosensory & Motor Research* **27**, 131–148 (2010).
9. Sanders, J. I. & Kepecs, A. Choice ball: a response interface for two-choice psychometric discrimination in head-fixed mice. *Journal of Neurophysiology* **108**, 3416–3423 (2012).
10. Hanks, T. D. & Summerfield, C. Perceptual Decision Making in Rodents, Monkeys, and Humans. *Neuron* **93**, 15–31 (2017).
11. Ashwood, Z. C. *et al.* Mice alternate between discrete strategies during perceptual decision-making. *Nat Neurosci* **25**, 201–212 (2022).

12. Nashaat, M. A., Oraby, H., Sachdev, R. N. S., Winter, Y. & Larkum, M. E. Air-Track: a real-world floating environment for active sensing in head-fixed mice. *Journal of Neurophysiology* **116**, 1542–1553 (2016).
13. Dominiak, S. E. *et al.* Whisking Asymmetry Signals Motor Preparation and the Behavioral State of Mice. *J. Neurosci.* **39**, 9818–9830 (2019).
14. Voigts, J. & Harnett, M. T. Somatic and Dendritic Encoding of Spatial Variables in Retrosplenial Cortex Differs during 2D Navigation. *Neuron* **105**, 237-245.e4 (2020).
15. Shadlen, M. N. & Kiani, R. Decision Making as a Window on Cognition. *Neuron* **80**, 791–806 (2013).
16. Marques, T. *et al.* A Role for Mouse Primary Visual Cortex in Motion Perception. *Current Biology* **28**, 1703-1713.e6 (2018).
17. Drugowitsch, J., Moreno-Bote, R., Churchland, A. K., Shadlen, M. N. & Pouget, A. The Cost of Accumulating Evidence in Perceptual Decision Making. *J. Neurosci.* **32**, 3612–3628 (2012).
18. Palmer, L. M. *et al.* The Cellular Basis of GABAB-Mediated Interhemispheric Inhibition. *Science* **335**, 989–993 (2012).
19. Hanks, T., Kiani, R. & Shadlen, M. N. A neural mechanism of speed-accuracy tradeoff in macaque area LIP. *eLife* **3**, e02260 (2014).
20. Dana, H. *et al.* Thy1-GCaMP6 Transgenic Mice for Neuronal Population Imaging In Vivo. *PLOS ONE* **9**, e108697 (2014).
21. Couto, J. *et al.* Chronic, cortex-wide imaging of specific cell populations during behavior. *Nat Protoc* **16**, 3241–3263 (2021).
22. Guo, Z. V. *et al.* Flow of Cortical Activity Underlying a Tactile Decision in Mice. *Neuron* **81**, 179–194 (2014).
23. Laubach, M., Amarante, L. M., Swanson, K. & White, S. R. What, If Anything, Is Rodent Prefrontal Cortex? *eNeuro* **5**, ENEURO.0315-18.2018 (2018).

24. Chen, T.-W., Li, N., Daie, K. & Svoboda, K. A Map of Anticipatory Activity in Mouse Motor Cortex. *Neuron* **94**, 866-879.e4 (2017).

25. Hanks, T. D. *et al.* Distinct relationships of parietal and prefrontal cortices to evidence accumulation. *Nature* **520**, 220–223 (2015).

26. Laubach, M., Wessberg, J. & Nicolelis, M. A. L. Cortical ensemble activity increasingly predicts behaviour outcomes during learning of a motor task. *Nature* **405**, 567–571 (2000).

27. Harvey, C. D., Coen, P. & Tank, D. W. Choice-specific sequences in parietal cortex during a virtual-navigation decision task. *Nature* **484**, 62–68 (2012).

28. Peters, A. J., Chen, S. X. & Komiyama, T. Emergence of reproducible spatiotemporal activity during motor learning. *Nature* **510**, 263–267 (2014).

29. Inagaki, H. K. *et al.* Neural Algorithms and Circuits for Motor Planning. *Annu. Rev. Neurosci.* **45**, 249–271 (2022).

30. Li, N., Daie, K., Svoboda, K. & Druckmann, S. Robust neuronal dynamics in premotor cortex during motor planning. *Nature* **532**, 459–464 (2016).

31. Akrami, A., Kopec, C. D., Diamond, M. E. & Brody, C. Posterior parietal cortex represents sensory history and mediates its effects on behavior. Preprint at https://doi.org/10.1101/182246 (2017).

32. Urai, A. E., De Gee, J. W., Tsetsos, K. & Donner, T. H. Choice history biases subsequent evidence accumulation. *eLife* **8**, e46331 (2019).

33. Notebaert, W. *et al.* Post-error slowing: An orienting account. *Cognition* **111**, 275–279 (2009).

34. Purcell, B. A. & Kiani, R. Neural Mechanisms of Post-error Adjustments of Decision Policy in Parietal Cortex. *Neuron* **89**, 658–671 (2016).

35. Thompson, K. G., Biscoe, K. L. & Sato, T. R. Neuronal Basis of Covert Spatial Attention in the Frontal Eye Field. *J. Neurosci.* **25**, 9479–9487 (2005).

36. Lak, A. *et al.* Reinforcement biases subsequent perceptual decisions when confidence is low, a widespread behavioral phenomenon. *eLife* **9**, e49834 (2020).
37. Gupta, D., DePasquale, B., Kopec, C. D. & Brody, C. D. Trial-history biases in evidence accumulation can give rise to apparent lapses in decision-making. *Nat Commun* **15**, 662 (2024).
38. Hirokawa, J., Vaughan, A., Masset, P., Ott, T. & Kepecs, A. Frontal cortex neuron types categorically encode single decision variables. *Nature* **576**, 446–451 (2019).
39. Scott, B. B. *et al.* Fronto-parietal Cortical Circuits Encode Accumulated Evidence with a Diversity of Timescales. *Neuron* **95**, 385-398.e5 (2017).
40. Roach, J. P., Churchland, A. K. & Engel, T. A. Choice selective inhibition drives stability and competition in decision circuits. *Nat Commun* **14**, 147 (2023).
41. Barthas, F. & Kwan, A. C. Secondary Motor Cortex: Where 'Sensory' Meets 'Motor' in the Rodent Frontal Cortex. *Trends in Neurosciences* **40**, 181–193 (2017).
42. Itokazu, T. *et al.* Streamlined sensory motor communication through cortical reciprocal connectivity in a visually guided eye movement task. *Nat Commun* **9**, 338 (2018).
43. Hanes, D. P. & Schall, J. D. Neural Control of Voluntary Movement Initiation. *Science* **274**, 427–430 (1996).
44. Cavanagh, J. F. *et al.* Subthalamic nucleus stimulation reverses mediofrontal influence over decision threshold. *Nat Neurosci* **14**, 1462–1467 (2011).
45. Murakami, M., Vicente, M. I., Costa, G. M. & Mainen, Z. F. Neural antecedents of self-initiated actions in secondary motor cortex. *Nat Neurosci* **17**, 1574–1582 (2014).
46. Frank, M. J., Doll, B. B., Oas-Terpstra, J. & Moreno, F. Prefrontal and striatal dopaminergic genes predict individual differences in exploration and exploitation. *Nat Neurosci* **12**, 1062–1068 (2009).
47. Yartsev, M. M., Hanks, T. D., Yoon, A. M. & Brody, C. D. Causal contribution and dynamical encoding in the striatum during evidence accumulation. *eLife* **7**, e34929 (2018).

48. Cowley, B. R. *et al.* Slow Drift of Neural Activity as a Signature of Impulsivity in Macaque Visual and Prefrontal Cortex. *Neuron* **108**, 551-567.e8 (2020).
49. Calderon, C. B., Verguts, T. & Frank, M. J. Thunderstruck: The ACDC model of flexible sequences and rhythms in recurrent neural circuits. *PLOS Computational Biology* **18**, e1009854 (2022).
50. Reppert, T. R., Heitz, R. P. & Schall, J. D. Neural mechanisms for executive control of speed-accuracy trade-off. *Cell Rep* **42**, 113422 (2023).
51. Leeuw, J. R. de, Gilbert, R. A. & Luchterhandt, B. jsPsych: Enabling an Open-Source Collaborative Ecosystem of Behavioral Experiments. *Journal of Open Source Software* **8**, 5351 (2023).
52. Rajananda, S., Lau, H. & Odegaard, B. A Random-Dot Kinematogram for Web-Based Vision Research. *Journal of Open Research Software* **6**, (2018).
53. Musall, S., Kaufman, M. T., Juavinett, A. L., Gluf, S. & Churchland, A. K. Single-trial neural dynamics are dominated by richly varied movements. *Nat Neurosci* **22**, 1677–1686 (2019).
54. Brainard, D. H. The Psychophysics Toolbox. *Spat Vis* **10**, 433–436 (1997).
55. Peirce, J. *et al.* PsychoPy2: Experiments in behavior made easy. *Behav Res* **51**, 195–203 (2019).
56. Pinto, L., Tank, D. W. & Brody, C. D. Multiple timescales of sensory-evidence accumulation across the dorsal cortex. *eLife* **11**, e70263 (2022).
57. Pachitariu, M. *et al.* Suite2p: beyond 10,000 neurons with standard two-photon microscopy. 061507 Preprint at https://doi.org/10.1101/061507 (2017).

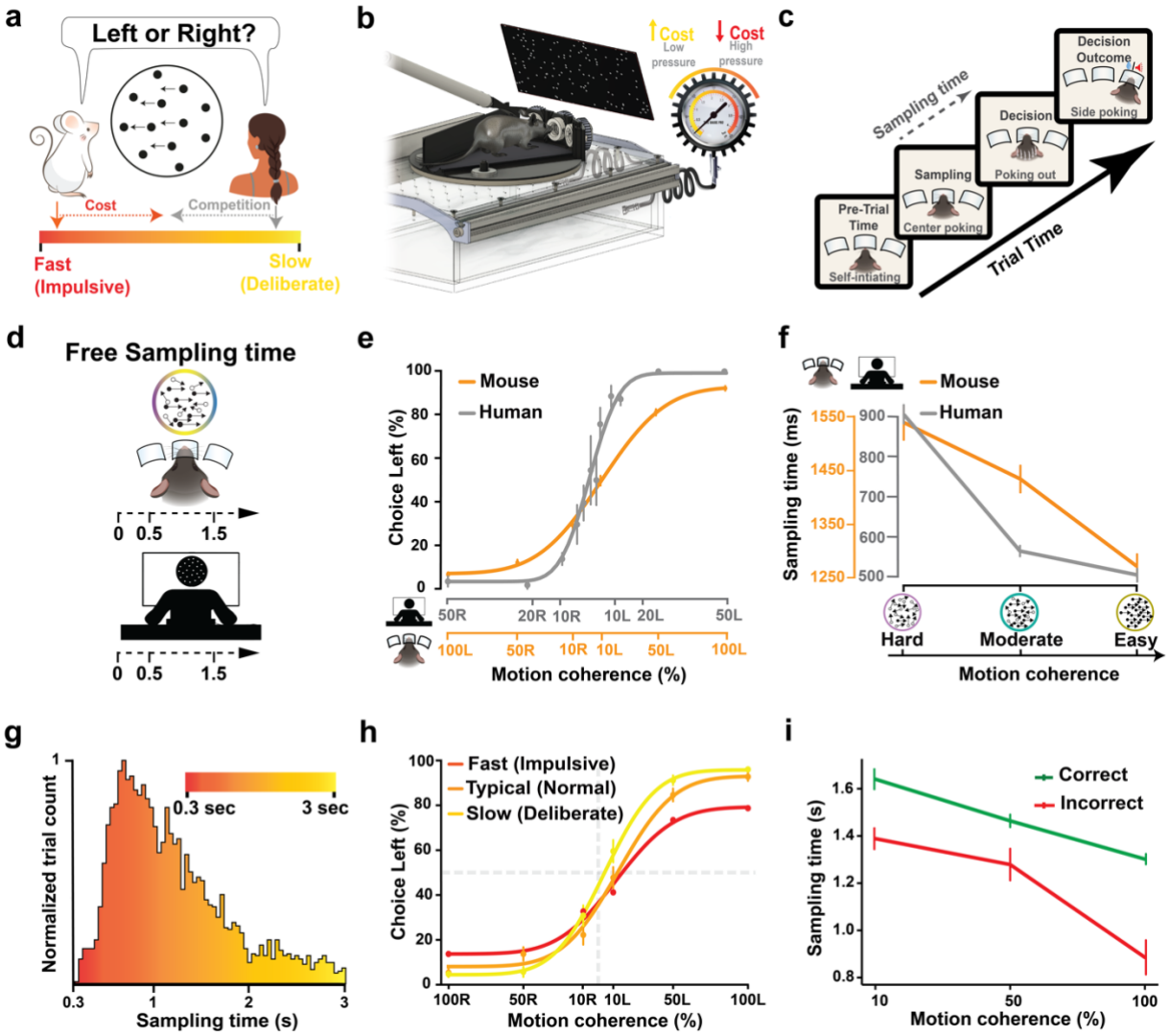

Figure 1. Novel behavioural approaches for investigating behavioural strategies in humans and head-fixed mice. a) Dynamic behavior in human and mice involved a range of both fast (impulsive) and slow (deliberate) decisions. b) 3D rendition of the floating-platform 3-port behavioural system allows cost manipulation of voluntary behaviour in head-fixed mice. c) Random Dots Kinematogram (RDK) task structure. d) Diagram of voluntary choice paradigm (free sampling-time) in both humans and mice. e) Psychometric function of human (gray) and mouse (orange) performance across different coherences (stimulus difficulties). Note: humans perform better because of their better visual motion acuity. f) Similar sampling times for both humans (gray) and mice (orange) across different levels of difficulty. g) Histogram of voluntary sampling times over 30 sessions in expert mice. h) Task performance (left-choice probability) as a function of task difficulty in both directions across different behavioural strategies (3 different sampling time quantiles from sampling time in g, consistent across difficulties (c.f: Extended Fig. 3d). i) Sampling time differs across difficulties during correct (green) versus incorrect (red) decisions.

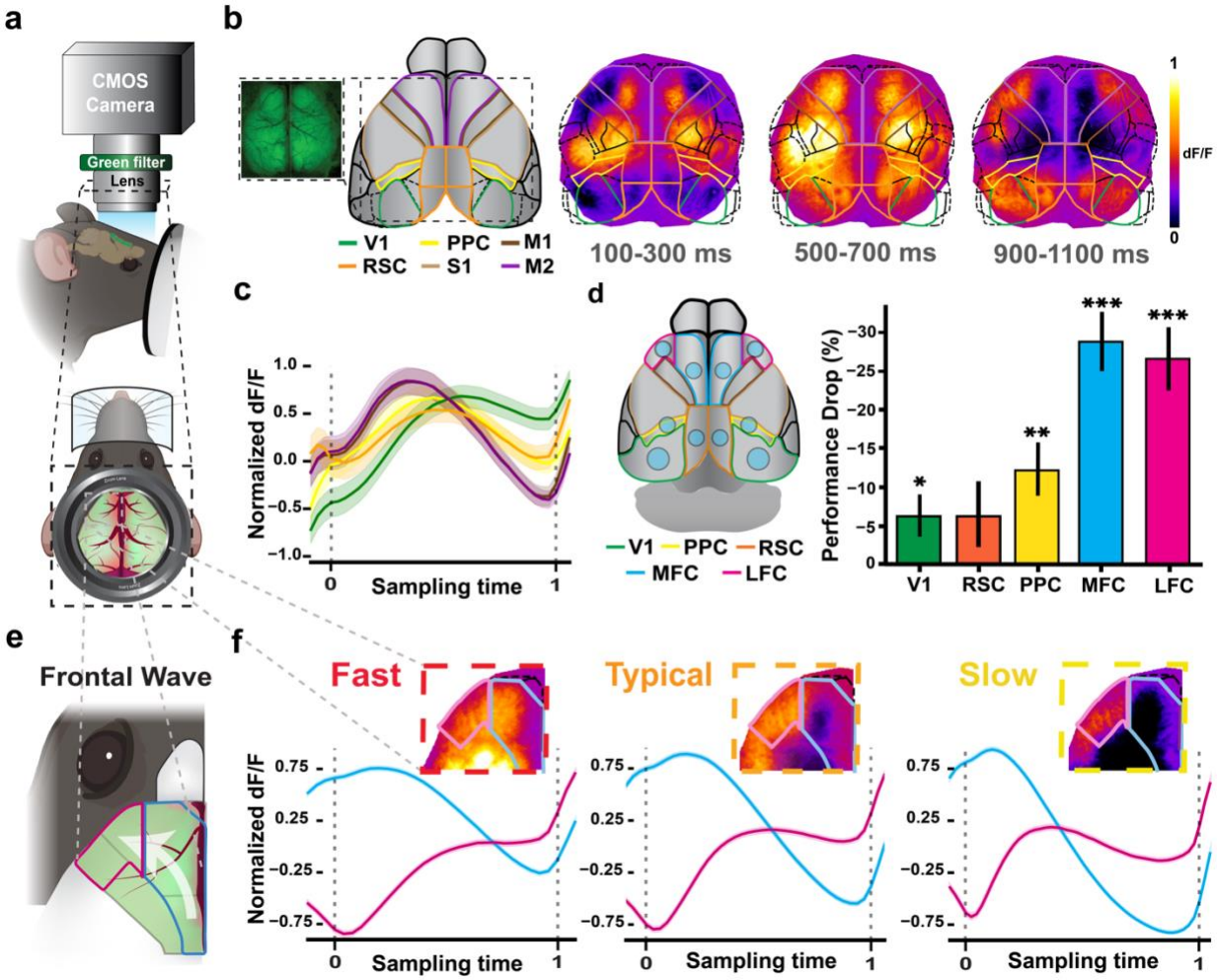

Figure 2. Medio-lateral activity wave in frontal cortex causally relates to decision making during different behavioural strategies. a) Schematic of widefield experimental setup. b) Average pixel-wise heatmap of calcium fluorescence from Thy1-GP4.3 (gCaMP6s) mice over three different sampling time windows in a typical sampling time RDK task. c) Averaged calcium activity from different cortical areas from b. d) Bilateral optogenetic silencing using a Vgat-Chr2 mouse of different cortical regions in a fixed, 1-s sampling-time task (areas labelled according to Allen brain atlas and the effect on performance). e) Functional segmentation of frontal area into medial frontal cortex (MFC, blue), and lateral frontal cortex (LFC, magenta), based on calcium wave dynamics (arrow). f) Average calcium fluorescence for frontal cortex across mice during different behavioural strategies, fast, typical, and slow behavioural trials.

441

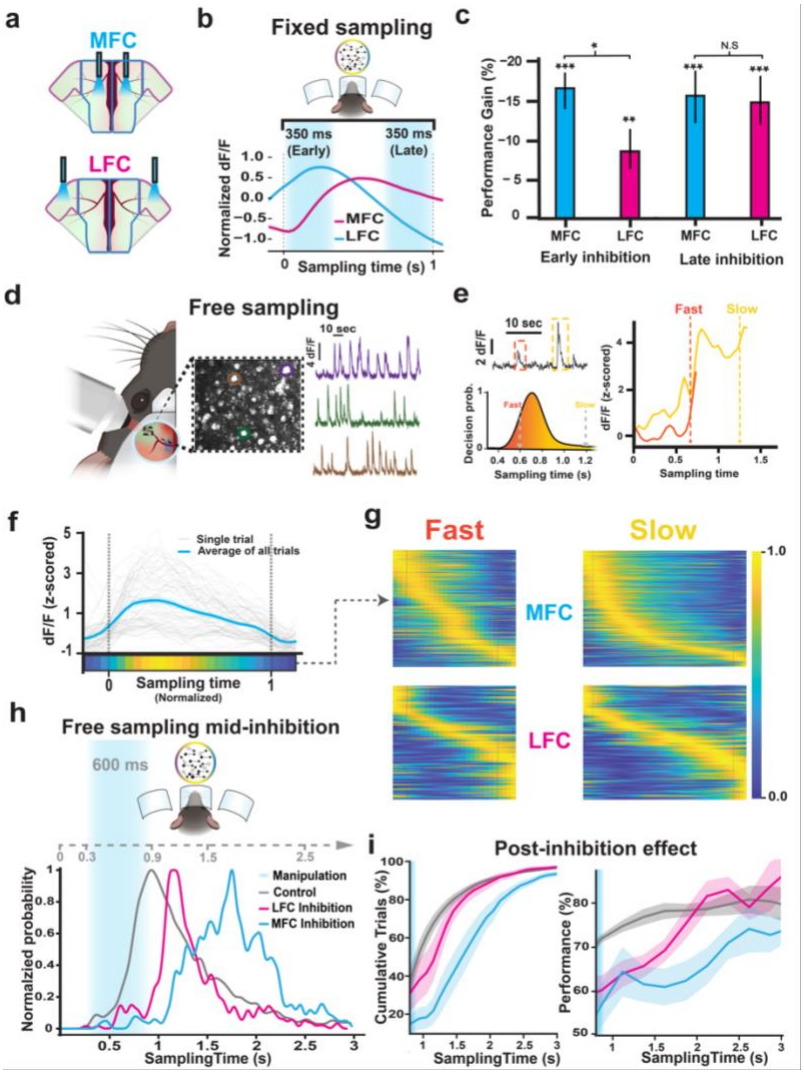

Figure 3. Optogenetic inhibition and two-photon imaging reveals distinct modes of operation in MFC and LFC. a) Schematic showing bilateral targeted inhibition of MFC and LFC. b) top, schematic of targeted inhibition within early (0-350ms) and late (650-1000ms) time-windows during fixed 1-s sampling-time task. Bottom, average frontal widefield calcium fluorescence. c) Effect on performance with optogenetic inhibition of frontal areas across early (0-350ms) and late (650-1000ms) time windows. d) Schematic diagram of two-photon imaging of calcium activity from layer 2/3 of mouse MFC & LFC. Middle panel, micrograph of neurons in imaged area. Right side, calcium activity traces (dF/F) from three different neurons colour-coded. e) Single-neuron calcium activity across sampling during different behavioural strategies extracted from raw dF/F traces. f) Average calcium activity from a single example neuron over sampling time (normalized) during impulsive behaviour from MFC (blue). Gray traces show normalized calcium responses for single trials. g) Heatmap responses from the neuronal population in MFC (top) and LFC (bottom) during fast (left) and slow (right) behavioural strategies. Neurons (heatmap lines) are ordered based on the average peak response (center of mass) during sampling (arrows indicate lines/neurons corresponding to examples on left). h) Schematic of optogenetic inhibition for MFC and LFC during free sampling paradigm (top). Bottom, sampling time distribution for control (gray), LFC inhibition (magenta), and MFC inhibition (blue) across sessions in an example mouse. i) Left, cumulative sampling time distribution for control trials (gray), MFC inhibition (blue), and LFC inhibition (magenta) across mice. Right, mice performance after the end of optogenetic inhibition timeline in control (gray), MFC (blue), and LFC (magenta).

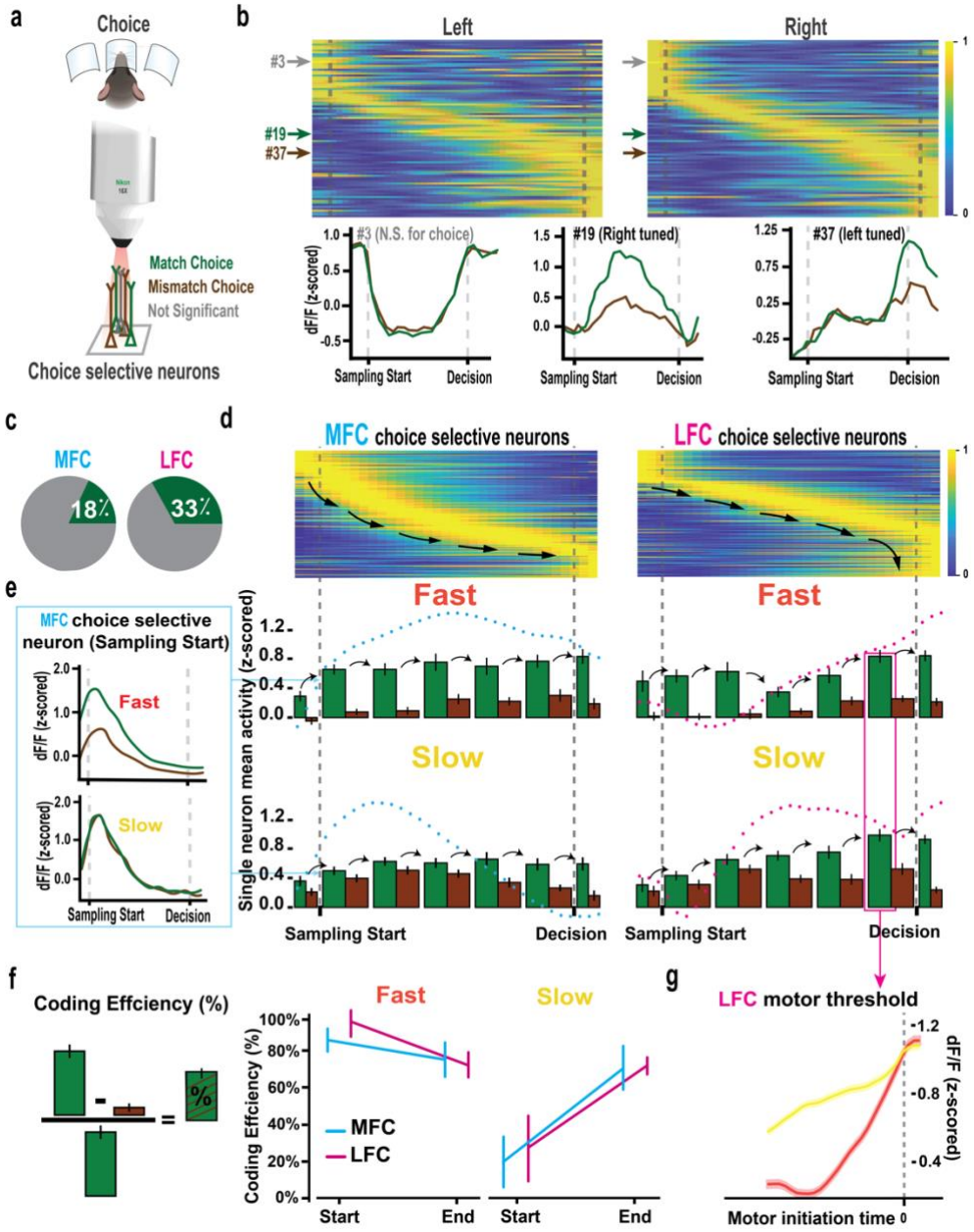

Figure 4. Sequence of choice selective neurons reflects the mechanism underlying behavioural strategy. a) Schematic for two-photon calcium imaging of L2/3 labeling choice selective neurons based on their responses to mouse choice. b) Heatmap of LFC showing sequence of active neurons firing over sampling isolated based on animal choice to left & right. Bottom panel, 3 example neurons showing similar response in both directions or significantly higher activity for a specific direction (left or right) during match trials. c) Pie chart showing the ratio of choice-selective neurons in MFC & LFC. d) Top, heatmap of choice-selective neurons in MFC (left) & LFC (right) across mice. Neural responses of sequence (arrows) choice-selective neurons according to peak activity for both matched (green) and mismatch trials over sampling in slow (middle panel) & fast (bottom panel) behavioural strategies. e) Example neuron from MFC choice-selective sequence (arrows) for match and mismatch mouse choice during fast and slow strategies. f) Right, coding efficiency is a measure for the separation of neural responses for matched and mismatched trials. Left, coding efficiency at the start and end of sampling for both MFC (blue) & LFC (magenta) across fast and slow behavioural strategies. g) Matched neurons' responses at the end of sampling in LFC sequence (pink box/arrow) for both fast and slow behaviour.

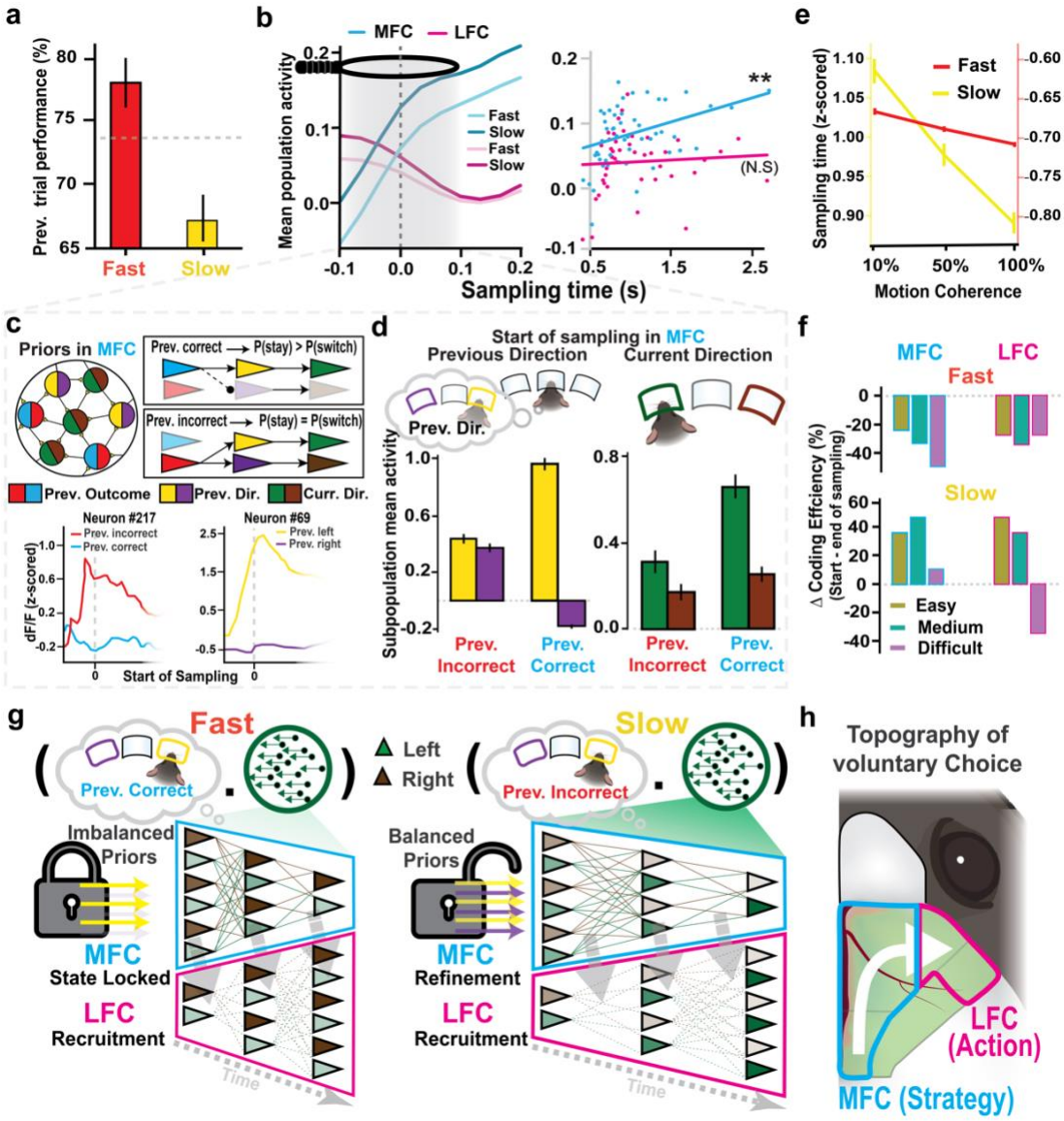

Figure 5. Priors and evidence shape strategy and action in distinct regions of mouse frontal cortex. a) The probability of fast and slow strategies as a function of previous correct outcome. b) Right, l2/3 population activity at the start of sampling in MFC (blue) and LFC (red) during fast and slow behavioural strategies (right). Left, Pearson correlation of the initial activity of MFC and LFC at the start of sampling as a function of sampling time. c) Top left, schematic showing single neurons at the start of sampling exhibit tuning to different decision relevant variables such as previous direction, previous outcome, and the current direction. Top right, schematic of neural mechanism by which previous trial outcome influences animal choice. Bottom, example neurons at the start of sampling in MFC exhibit selectivity for previous outcome (left), and previous direction (right). d) The influence of previous outcome on neurons selective for previous choice direction (left) and current choice direction (right) at the start of sampling in MFC. e) Normalized sampling time as a function of stimulus difficulty (evidence) during fast (red) and slow (yellow) decisions. f) The difference in coding efficiency between start of sampling and end of sampling during sampling different stimulus difficulties during fast and slow behavioural strategies. g, h) Schematic of frontal mechanism during voluntary decision making that involves the interaction between the medial and lateral frontal cortices including different decision relevant variables guiding fast and slow behavioural strategies.

Methods

Human psychophysical Experiment

The study was conducted in Humboldt university recruiting 33 participants and approved by the local ethics committee of the Humboldt University Berlin.

University students constituted the pool of participating subjects. The experiment was conducted in three group sessions, each involving 10-12 subjects who were assigned a computer rig (Optiplex 7400 AIO Series). Subjects were made aware of the scoring criteria and were encouraged to compete for the highest score. Most users ran both accuracy and maximum correct outcome experiments, with each experiment duration set to 30 minutes including a 5-minute break at the 15-minute mark, as well as a mandatory 20-second break every 100 trials. Subjects performed an initial 10 test trials. For the accuracy competition, a subject's score is calculated as the percentage of correct trials over the total trials, with a minimum requirement of 50 trials. For the maximum correct outcome competition, the subject's score is the total number of correct trials. A central server controlled by the experimenter activated a countdown timer to synchronize the start of the session on all subjects' computers, thus ensuring all subjects are participating concurrently. Subjects received correct/incorrect feedback after each trial and could track their ranking among other players, viewing the leaderboard during individual 20-second breaks and the 15-minute group break. The experiments were implemented using jsPsych: and utilizing the jspsych-rdk plugin[51,52]. The stimulus comprised of 1,000 white dots on a black background, with a dot size of 0.3 pixels and a dot lifetime of 1 second.

Mice Experiments

All experiments were conducted in accordance with the guideline given by Landesamt für Gesundheit und Soziales Berlin and were approved by this authority.

Surgeries

We used adult (>P40) C57BL/6 wild-type mice, GP4.3Cre thy1, (#:024275, The Jackson laboratory), and VGAT-CHR2-EYE transgenic mice (#:014548, The Jackson laboratory). Mice were anaesthetized with mit Ketamin/Xylazin (Ketamin 12,5 mg/ml, Xylazin 1 mg/ml (10 µl/g) intraperitoneal) and kept on a thermal blanket. After surgery,mice received Caprofen (5 mg/kg) und Buprenorphin (0,05-0,1 mg/kg) for 2 days. During head-fixation skin and periosteum were removed, a thin layer of light-curing adhesives was applied to the skull. A light-weight head-post was fixed on the skull with a dental cement. For widefield imaging, intact skull cleared using a layer of cyanoacrylate (Zap-A-Gap CA+, Pacer technology) to clear the bone[53]. Green fluorescent was check under widefield microscope after surgery and double checked later with two-photon imaging calcium imaging. For optogenetics, over intact skull stereotaxic marks were identified using permanent marker, before skull clearing, to label different targets of optogenetic inhibtion: primary visual cortex, V1 (1.0 mm anterior to lambda and 3 mm lateral from the midline), retrosplenial cortex, RSC (1.0 mm anterior to lambda and 0.7 mm lateral from the midline),

posterior parietal cortex, PPC (2.0 mm anterior to lambda and 2 mm lateral from the midline), Medial Frontal Cortex, MFC(0.8 mm anterior to bregma and 0.7 mm lateral from the midline), LFC, LFC (2 mm anterior to lambda and 1.8 mm lateral from the midline). For two photon imaging, a 3-mm craniotomy was made 0.3mm radially anterior from bregma and sealed with a 3-mm glass coverslip with cyanoacrylate glue and dental cement.

Behaviour

Behavioural Setup

Our behavioural studies employed a modification for the setup developed by Nashaat et al. 2016, that allows integrating natural behaviours with advanced neuroimaging in a head-fixed context. The setup is composed of a Plexiglas air-table, perforated with evenly spaced holes, rerdirecting compressed air to generate an upward current flow, levviating a PLA platform (15cm diameter) on top. The platform features 3 nose-pokes allowing the mice to navigate and seek rewards. A head-fixation mechanism ensures the mouse's head remains centered. The nose pokes, equipped with LEDs, infrared sensors, and a reward delivery tube, controlled by a solenoid valve, are extension of the Bpod (Sanworks) behavioral control system. To display RDK stimuli, a Retina LCD screen was positioned in front of the platform, approximately 10-15 cm away. RDK stimulus was generated with custom script utilizing either Psychtoolbox or Psychopy[54,55].

Behavioural Training

The initial phase introduced freely moving mice to the behavioral system using a simple light-chasing task conducted over three sessions, each approximately 30 minutes. This phase allowed the mice to acclimate to the environment and task structure. In this task, trials began with the mice fixing their nose inside the central port, illuminated first, followed by a light cue on either the left or right port signaling the correct choice. A successful selection resulted in a water-based reward, sweetened with 0.05% saccharine and sucralose, while incorrect choices triggered a high-pitched beep (4000-5000 Hz) as negative feedback. Subsequently, mice were head-fixed to adapt to moving the platform themselves, guided by experimenter-assisted platform movements. As mice perform above 75% accuracy in light-chasing task, a 4-seconds timeout penalty for incorrect choices is introduced. Trials where mice exited the central port before minimum sampling resulted in aborted trial with 1-2 second timeout. Expert-level was marked by sustained >75% accuracy across sessions, after which RDK stimuli were gradually integrated alongside light cues. Initially paired, the reliance on light cues was reduced until the task relied solely on RDK stimuli, with varying coherence levels (100%, 50%, 10%) introduced as the training advanced. Motion direction and coherence varied pseudo-randomly to prevent biases.

Fixed sampling Paradigm

For the fixed time (FT) Paradigm, the approach mirrored tasks previously conducted[10,15,16]. In FT trials, Mice must remain poked-in for the entire 1s stimulus presnetation duration. Early-Withdrawals counted as aborted trials. For the chronometry experiment (Extended Fig. 1c), trials between 0.3s to 1.2s, in increments of 0.3s, were presented in pseudo-random order with 20% probability in-between 1s trials.

Free sampling Paradigm

For free sampling paradigm, the approach mirrored tasks previously conducted with humans and monkeys. In this paradigm, the stimulus is continously presented and only terminated on exiting the center port, with a maximum of 5s cap. The mice had the autonomy to end the sampling period anytime between a minimum of 0.3s and a maximum of 5s, facilitating a balance between impulsivity control and decision-making flexibility. Trials with less than 0.3s sampling duration are counted as aborted trials.

Optogenetics

The targeting coordinates for optogenetic inactivation were determined using the Allen Brain Map API for Mouse Brain data[22,56]. 473-nm laser (OEM Laser Systems) was administered through bifurcated fiber bundle (Thorlabs BFYL2LF01), each emitting light covering approximately 250 μm in diameter at a 40 Hz with an 80% duty cycle and an intensity of 6 mW/mm² to ensure that photoinhibition was confined to the targeted cortical areas[22]. Additionally, blue masking light was positioned above the viewing screen. Training data indicated that mice exposed only to the masking light maintained an average performance exceeding 75%. In each experimental session, mice experienced perturbation in one brain area per session, with optogenetic trials pseudorandom introduced among control trials. To sustain high performance levels (70% or higher) and avoid demotivation, the probability of light illumination was set at 15-20%. During optogenetic inactivtion under fixed-time paradigm, inactivation duration was either throughout the entire delivery period (1s, Full), during the early (0-0.35s, Early), or the late (0.65-1s, Late) phases of stimulus presentation (Figure 2)[25].

Widefield imaging

We used an adaptation of widefield imaging setup that utilizes two light source for hemodynamic responses correction. We used the following variation: for the inverted tandem lens macroscope, we utilized a top lense with focal length, 105 mm (DC-Nikkor, Nikon) and a bottom one with focal length 85 mm (85M-S, Rokinon)[21,53].

Two-Photon Calcium Imaging

Imaging utilized a resonant-scanning two-photon microscope (ThorLabs B-scope) at a 5 kHz scanning rate. GCaMP6s excitation occurred at 940 nm via a Ti: Deepsee laser (90-110 mw power). Data collection was through a 16x water immersion objective (Nikon, 0.8 NA), capturing 512 x 512 pixel full-frame images of layer II/III neurons within a 1 mm² area, at 150-300 μm depths. Selection criteria for imaging fields included cell density and

minimal vascular interference. Imaging operated at 30 Hz frame rate, employing ThorImage software.

Data Analysis

Data analysis was performed using Python utilizing Numpy, Scipy, Pandas Scikit-Learn, Matplotlib, Seaborn and stats models libraries.

Human and Mice Behavioral Analysis

Each trial was classified as fast, typical or slow. Classification was assigned after dividing each animal's session to the 3 difficulties and splitting each difficulty to 3 quantiles (1st Quantile: Fast, 2nd Quantile: Typical, 3rd Quantile: Slow). Early-Withdrawal trials and trials where mice animal remained in the poke after the end of 5 seconds stimulus presentation during free-sampling paradigm time were excluded. In analyses where reaction-time Z-score normalization is applied, each mouse's data was normalized across all sessions. Mice with few trials or that followed a non-typical strategy, dissimilar to Fig. 1i, were excluded (21,628 out of 90,973 Trials were excluded).

The drift-diffusion model simulation (Extended Fig. 2e-f) was implemented using the PyDDM library (https://github.com/mwshinn/PyDDM).

For Extended Fig. 3b-c, mice and human subjects were limited to a maximum sampling time of 3 seconds to exclude trials where human subjects did not complete trials and to exclude large mean-values skews in mice data. All groups were compared using one-way ANOVA, followed by Tukey's test with Bonferroni correction for post-hoc pairwise comparisons. In Extended Fig. 12b, groups were compared using the Kruskal-Wallis test, with post-hoc comparisons performed using Dunn's test with Holm–Bonferroni correction. For Extended Fig. 12c, Z-score normalized sampling times were pooled and classified as Win (previous trial correct) or Lose (previous trial incorrect). Each classification was split into bins of 800 trials each, where the stay/switch update was calculated relative to the system-generated baseline stay/switch distribution for the bin, and a Gaussian kernel was applied to smooth changes between neighboring bins. Two mice were excluded due to abnormal quick responses. The stay/switch update per sub-panel in Extended Fig. 12d was calculated similarly to a single bin calculation in Fig. 12b. In Extended Fig. 14c, the change in sampling time between the current and previous trials was calculated after offsetting the sampling times by the mean sampling time of the respective trial difficulty. Psychometric curves were fit using the Psychofit library (https://github.com/cortex-lab/psychofit) with an error function and a two lapse-rate configuration, with trial difficulties binned in power of two increments.

Optogenetics Data Analysis

Optogenetics data was collected for one brain-region at a time and its control trials span between the first and last brain-region optogenetics trials. To quantify the optogenetics

performance effect, we computed the drop in performance across each session as follows:

$$Drop = 100 \times \left(\frac{\overline{Opto\ Performance}}{\overline{Control\ Perfomance}} - 1 \right)$$

To test whether optogenetics inhibition effect is significant, we ran paired two-tailed t-test on each of control and optogenetics mean performance pair. Wilcoxon–Mann–Whitney two-sided test was used to compare whether the performance effect of optogenetics inhibition significantly differs between two brain regions (Fig 3 c).

To regress the relation between sampling time and performance under control and optogenetics inhibition conditions (Extended Fig.10c), we performed linear regression on the z-score normalization on the sampling time of each animal control session. The optogenetics trials were z-score transformed using the corresponding control data distribution. To acquire mean performance, trials were grouped in bins of 50 trials. A linear fit for each of the control and optogenetics sessions as well as the overall data were plotted using a fixed common origin value at -1.5 z-score and 50% performance.

Wide-Field Imaging Data Analysis

We adapted a variation of the analysis in (https://github.com/jcouto/wfield) with the following changes: using 800 singular value decomposition (SVD) components; after the registration step we set pixels outside the brain to black to minimize their assigned SVD weights; and we used separate left and right hemispheres for a better fit in order to account for unequal sizes due to zooming artifacts[21].

Two-Photon Data Analysis

Preprocessing

Raw two-photon imaging data were preprocessed using Suite2p for image registration and neurons extraction followed by manual inspection[57].

To identify active neurons and neurons active trials, we adapted a variation of the steps used in previous 2 photon imaging studies[39]. We extracted raw traces 0.1 seconds before start of sampling until 0.1 seconds after end of sampling. For each trace, a z-score normalization is temporarily applied across a concatenation of all the sampling trials. Each trial is re-extracted, and the standard deviation is computed after applying a 1-frame gaussian smoothing. A neuron is marked to have an active trial its trace standard deviation within the trial exceeds a threshold value of 3 x 5th percentile of all the trials standard deviation. Neurons with less than 5 percent active trials are discarded. 837 out of 2,340 neurons in MFC (36.44% ±6.9%SD per session), while 609 out of 1,0536 neurons were marked as active in LFC (38.88% ±7.51%SD per session).

Neurons $\Delta F/F_0$ was calculated using the whole session trace after applying a 1-frame gaussian smoothing. F_0 is computed by computing the mode value of all the frames

baseline. A frame's baseline was computed as the maximum of the minimum values in the surrounding 60 seconds' window.

Heatmaps

In Fig 3g, each heatmap was sorted and normalized its activity in reference to its own data. In Fig 3b, slow left and right trials heatmaps were sorted according to a common sort of all slow trials heatmap, while each neuron activity is normalized to the minimum and maximum across the left and right trials choices heatmaps. Fig 3d top contains choice selective neurons (see tuning selectivity section) pooled across all brain-region sessions.

Tuning Selectivity

To test neurons selectivity for a criterion, e.g (previous) left/right choices, easy/difficult trials and previous correct/incorrect outcomes, trials maximum activity for each condition is extracted and are compared using Wilcoxon–Mann–Whitney two-sided significance test.

Sequence Characterization

To identify neurons' rank within a sequence, we use the median value of each neuron peak firing position during its active trials within time normalized trials.

To test the consistency of neurons sequence firing across trials (Extended Fig. 8b), we discarded neurons with less than 10% active trials, as few neurons might have low activity under one strategy and none in the others. For each session, the rank of neurons median peak firing position during typical trials was used as reference position. We tested the neurons rank for each of the fast and slow strategies against a 100,000 runs of typical trials rank permutations. Each run was assigned a penalty score:

$$\text{Penalty} = \frac{\sum|\text{neuron new rank} - \text{reference rank}|}{Number\ of\ neurons}$$

In comparison to the z-score penalty distribution of permutation runs, all of MFC sessions (n=13) were significantly different than permutation for both fast (mean z-score penalty= -6.8 ±2.51 Std. P-value < 0.001), and slow (mean z-score penalty=-6.83 ±2.21 Std., P-value < 0.001), while for LFC, all of the fast sequences (n=10) were significantly different than permutation (mean z-score penalty=-6.53 ±1.77 Std., P-value < 0.001), where most of slow sequences were significantly different (9/10 sessions, mean z-score penalty=-6.24 ±2.34 Std., P-value < 0.001).

To further quantify the change in peak firing positions across trials of each strategy, we plotted a histogram (Extended Fig. 8e bottom) of the distance that neurons span across normalized trial time to cover the IQR boundaries. Across MFC and LFC and across the behavioral strategies, the majority of neurons IQR span 0 → 0.3 normalized time with mode histogram value of 0.2 seconds normalized time.

In Fig. 3d bottom, each pair of bins contains the set of choice significant neurons pooled across all brain-region sessions that their peak firing position IQR fall within the bin-pair boundary. Each pair of green and brown bins contain the same set of neurons under different trial conditions: when the trial matches the neuron selectivity (green) and when trial mismatches it (brown). The bin height and error bar reflect the average and SEM of the neurons mean z-score activity under the bin condition. We split time-normalized sampling duration into 7 bins pairs: boundaries pair before and after sampling start/end and 5 equal-time pairs during sampling. We excluded neurons that their median peak firing position falls within the first and last bins pairs, to avoid including predominantly motor tuned neurons.

To further confirm the observed effects, a logistic-regression choice classifier was run on significant choice neurons. After applying z-score normalization to the sampling epoch, the features input to the classifier is each significant neuron maximum firing at each trial at either the start of sampling (0.1 before and 0.2 after start of sampling) or end of sampling (0.2 before and 0.1 after end of sampling). The classifier input labels are the animal direction choice. For each test combination, a 1,000 of random training and test splitting is performed, with 30% of the data used for testing on each run.

We defined Coding-efficiency, a measure of the mean separation between match and mismatched selectivity, as follows:

$$Eff = \frac{\overline{\text{Match}} - \overline{\text{Mismatch}}}{\overline{\text{Match}}}$$

Coding-efficiency error bars are computed using the propagation of uncertainty approximation method:

$$\Delta Eff = \sqrt{\left(\frac{100 \cdot \overline{\text{Match}} - 100 \cdot \left(\overline{\text{Match}} - \overline{\text{Mismatch}}\right)}{\overline{\text{Match}}^2}\ \sigma_{\text{Match}}\right)^2 + \left(\frac{-100}{\overline{\text{Match}}}\ \sigma_{\text{Mismatch}}\right)^2}$$

To describe a two-photon population activity, either the mean activity of all neurons (Fig. 4d bottom dotted lines, Fig. 3b left, Extended Fig. 9b-c right, and Extended Fig. 16a), or the mean activity of only significant neurons (Fig. 4g and Extended Fig. 14a) is computed across each time point. In Fig. 5b right, we fit a linear regression of z-score normalization of each session sampling time against the mean initial activity during the sampling initial activity (0.1 before to 0.1 seconds after the start of the sampling period). In both Fig. 5b right and the corresponding Extended Fig. 13a, trials are binned in 0.2 z-score increments such that a non-binary mean performance value can be computed. Bins with less than 50 trials were discarded.

Figure Legends

Figure 1. Novel behavioural approaches for investigating behavioural strategies in humans and head-fixed mice. a) Dynamic behavior in human and mice involved a range of both fast (impulsive) and slow (deliberate) decisions. b) 3D rendition of the floating-platform 3-port behavioural system allows cost manipulation of voluntary behaviour in head-fixed mice. c) Random Dots Kinematogram (RDK) task structure. d) Diagram of voluntary choice paradigm (free sampling-time) in both humans and mice. e) Psychometric function of human (gray) and mouse (orange) performance across different coherences (stimulus difficulties). Note: humans perform better because of their better visual motion acuity. f) Similar sampling times for both humans (gray) and mice (orange) across different levels of difficulty. g) Histogram of voluntary sampling times over 30 sessions in expert mice. h) Task performance (left-choice probability) as a function of task difficulty in both directions across different behavioural strategies (3 different sampling time quantiles from sampling time in g, consistent across difficulties (c.f: Extended Fig. 3d). i) Sampling time differs across difficulties during correct (green) versus incorrect (red) decisions.

Figure 2. Medio-lateral activity wave in frontal cortex causally relates to decision making during different behavioural strategies. a) Schematic of widefield experimental setup. b) Average pixel-wise heatmap of calcium fluorescence from Thy1-GP4.3 (gCaMP6s) mice over three different sampling time windows in a typical sampling time RDK task. c) Averaged calcium activity from different cortical areas from b. d) Bilateral optogenetic silencing using a Vgat-Chr2 mouse of different cortical regions in a fixed, 1-s sampling-time task (areas labelled according to Allen brain atlas and the effect on performance). e) Functional segmentation of frontal area into medial frontal cortex (MFC, blue), and lateral frontal cortex (LFC, magenta), based on calcium wave dynamics (arrow). f) Average calcium fluorescence for frontal cortex across mice during different behavioural strategies, fast, typical, and slow behavioural trials.

Figure 3. Optogenetic inhibition and two-photon imaging reveals distinct modes of operation in MFC and LFC. a) Schematic showing bilateral targeted inhibition of MFC and LFC. b) top, schematic of targeted inhibition within early (0-350ms) and late (650-1000ms) time-windows during fixed 1-s sampling-time task. Bottom, average frontal widefield calcium fluorescence. c) Effect on performance with optogenetic inhibition of frontal areas across early (0-350ms) and late (650-1000ms) time windows. d) Schematic diagram of two-photon imaging of calcium activity from layer 2/3 of mouse MFC & LFC. Middle panel, micrograph of neurons in imaged area. Right side, calcium activity traces (dF/F) from three different neurons colour-coded. e) Single-neuron calcium activity across sampling during different behavioural strategies extracted from raw dF/F traces. f) Average calcium activity from a single example neuron over sampling time (normalized) during impulsive behaviour from MFC (blue). Gray traces show normalized calcium responses for single trials. g) Heatmap responses from the neuronal population in MFC

743 (top) and LFC (bottom) during fast (left) and slow (right) behavioural strategies. Neurons
744 (heatmap lines) are ordered based on the average peak response (center of mass) during
745 sampling (arrows indicate lines/neurons corresponding to examples on left). h) Schematic
746 of optogenetic inhibition for MFC and LFC during free sampling paradigm (top). Bottom,
747 sampling time distribution for control (gray), LFC inhibition (magenta), and MFC inhibition
748 (blue) across sessions in an example mouse. i) Left, cumulative sampling time distribution
749 for control trials (gray), MFC inhibition (blue), and LFC inhibition (magenta) across mice.
750 Right, mice performance after the end of optogenetic inhibition timeline in control (gray),
751 MFC (blue), and LFC (magenta).

752 **Figure 4. Sequence of choice selective neurons reflects the mechanism underlying**
753 **behavioural strategy.** a) Schematic for two-photon calcium imaging of L2/3 labeling
754 choice selective neurons based on their responses to mouse choice. b) Heatmap of LFC
755 showing sequence of active neurons firing over sampling isolated based on animal choice
756 to left & right. Bottom panel, 3 example neurons showing similar response in both
757 directions or significantly higher activity for a specific direction (left or right) during match
758 trials. c) Pie chart showing the ratio of choice-selective neurons in MFC & LFC. d) Top,
759 heatmap of choice-selective neurons in MFC (left) & LFC (right) across mice. Neural
760 responses of sequence (arrows) choice-selective neurons according to peak activity for
761 both matched (green) and mismatch trials over sampling in slow (middle panel) & fast
762 (bottom panel) behavioural strategies. e) Example neuron from MFC choice-selective
763 sequence (arrows) for match and mismatch mouse choice during fast and slow strategies.
764 f) Right, coding efficiency is a measure for the separation of neural responses for matched
765 and mismatched trials. Left, coding efficiency at the start and end of sampling for both
766 MFC (blue) & LFC (magenta) across fast and slow behavioural strategies. g) Matched
767 neurons' responses at the end of sampling in LFC sequence (pink box/arrow) for both fast
768 and slow behaviour.

769 **Figure 5. Priors and evidence shape strategy and action in distinct regions of**
770 **mouse frontal cortex.** a) The probability of fast and slow strategies as a function of
771 previous correct outcome. b) Right, l2/3 population activity at the start of sampling in MFC
772 (blue) and LFC (red) during fast and slow behavioural strategies (right). Left, Pearson
773 correlation of the initial activity of MFC and LFC at the start of sampling as a function of
774 sampling time. c) Top left, schematic showing single neurons at the start of sampling
775 exhibit tuning to different decision relevant variables such as previous direction, previous
776 outcome, and the current direction. Top right, schematic of neural mechanism by which
777 previous trial outcome influences animal choice. Bottom, example neurons at the start of
778 sampling in MFC exhibit selectivity for previous outcome (left), and previous direction
779 (right). d) The influence of previous outcome on neurons selective for previous choice
780 direction (left) and current choice direction (right) at the start of sampling in MFC. e)
781 Normalized sampling time as a function of stimulus difficulty (evidence) during fast (red)
782 and slow (yellow) decisions. f) The difference in coding efficiency between start of
783 sampling and end of sampling during sampling different stimulus difficulties during fast

784 and slow behavioural strategies. g, h) Schematic of frontal mechanism during voluntary
785 decision making that involves the interaction between the medial and lateral frontal
786 cortices including different decision relevant variables guiding fast and slow behavioural
787 strategies.

Extended Figures

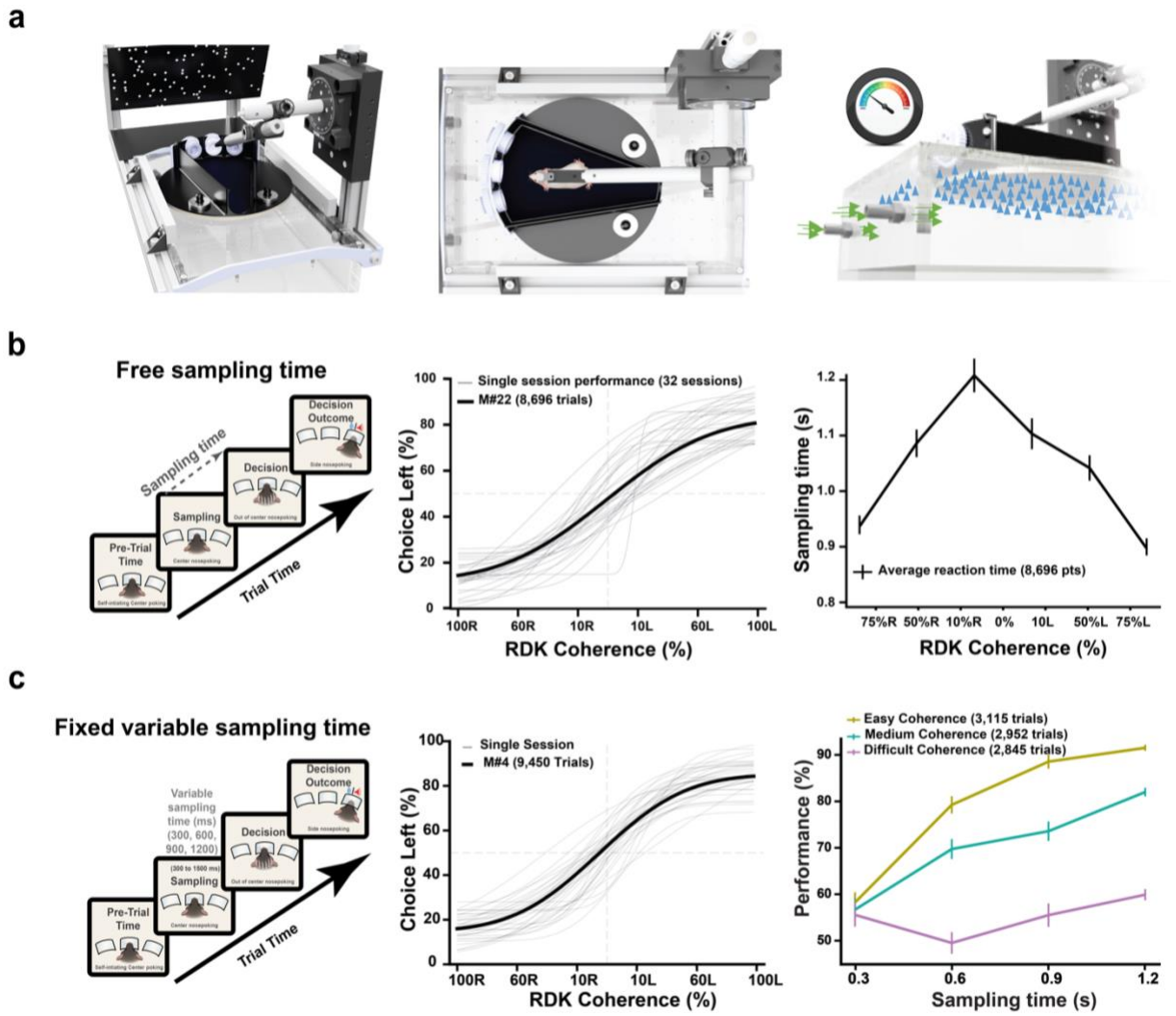

Extended Figure 1. Novel nose-poke floating-platform approach to study mechanisms of cognitive in mice. a) 3D rendition of sideview (left), top view (middle), and bottom view (right) of nose-poke floating-platform for head-fixed mice performing Random Dots Kinematogram (RDK) task. b) Structure for free sampling RDK task (left), psychometric performance for an example mouse over sessions (middle), and average sampling time across different coherences for right and left choices (right). c) Task structure for fixed variable sampling time in RDK task (left), psychometric performance for an example mouse over sessions (middle), and mouse performance across different difficulties during different fixed variable sampling time (right).

We developed a nose-poke floating platform that enables the transfer almost any freely moving behavioural paradigm mice to head-fixation. This facilitates imaging and recording techniques investigating neural activity at both cellular and subcellular scales. We designed a 2AFC task using 3 nose-pokes while a screen stands in front of the head-fixed mice discriminating the moving direction of Random Dots kinematics (RDK) (Extended Fig. 1a). By allowing air to flow out of the pores of the air-table, an air cushion underneath the platform facilitate moving the platform smoothly. Mice can move the platform with little friction to execute a trial. Mice learn to center-poke to initiate a trial and move the platform toward the side-poke direction that matches the majority of the dot's

movement direction. We trained head-fixed mice to voluntarily sample RDK stimulus exhibiting high accuracy at high motion coherences (100%) and a chance level performance at low motion coherence (10%) (Extended Fig. 1b). Like humans, head-fixed mice voluntarily sampled low coherence RDK stimulus more than high coherence RDK stimulus. We also trained head-fixed mice to make a decision after a fixed sampling time (Extended Fig. 1c). By variably changing fixed sampling time on trial-by-trial basis, ranging from 300 ms, 600ms, 900ms and 1200 ms, head-fixed mice chronometry curve showed that mouse perform with higher accuracy the longer it samples the RDK stimulus.

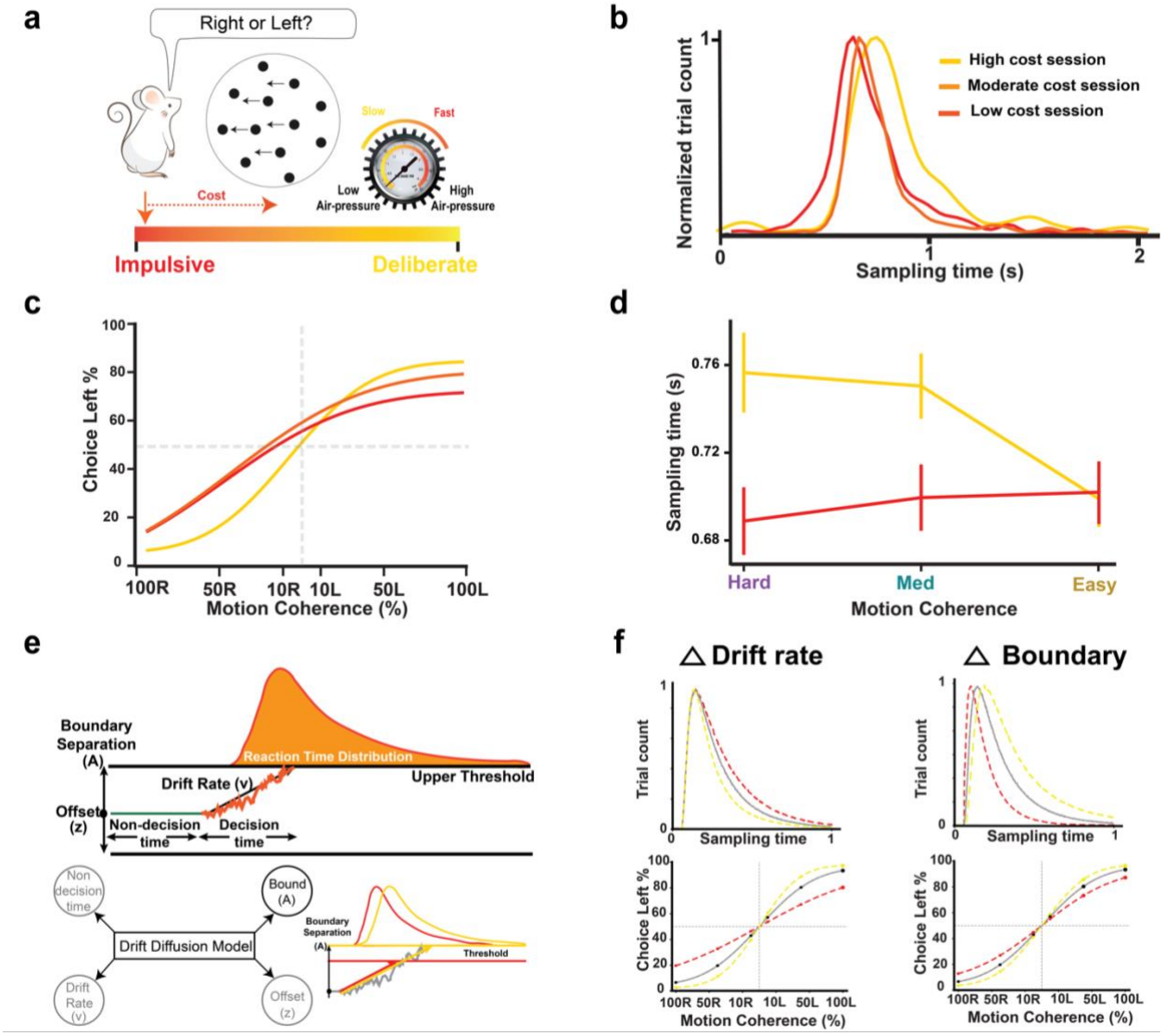

Extended Figure 2. Cost manipulation in nose-poke floating-platform increase sampling time and performance. a) Schematic showing dynamic sampling strategy in mice using nose-poke floating platform involved a range of fast and slow decisions that can be manipulated by changing airflow (cost). b) Changing the cost of making a choice shifts sampling time distribution from a session to another. Sessions with longer sampling time distribution exhibit better performance (c) and adaptive optimal sampling strategy across difficulties (d). e) Top, schematic of drift diffusion model (DDM) and, bottom right, basic elements that controls a DDM based decision making process. f) Changing different parameters of DDM such as drift rate (left) and Boundary (right) with consequent effect on both sampling time and with performance. Out of the four basic DDM parameters, only changes in boundary (threshold) leads to a combined increase in sampling time and performance.

The floating platform provides a unique opportunity to change airflow and accordingly the smoothness (less-friction) of moving the platform (Extended fig. 2a). Changing the amount of air flowing through the pores of the air-table was generally a useful tip to guide animal during early phase of head-fixation as high air-pressure helps the animal move the platform. Meanwhile, when the animal can smoothly move the system showing impulsive behaviour due to water deprivation, turning the air-pressure down makes the animal sample longer and improve learning and performance. Even in a trained mouse changing the airflow (the cost of making a choice) affects the distribution of stimulus

sampling time and decision accuracy on session-by-session basis. In comparison to high airflow, decrease airflow shifts sampling time distribution to the left and lead to shallower psychometric curve (Extended fig. 2b, c). At high cost, mice use an optimal strategy by sampling more for difficult trials and less for easy trials (Extended fig. 2d). In order to understand the impact of airflow on the process of decision making. We exploit basic drift diffusion model (DDM) parameters used to describes voluntary decision making in RDK stimulus (i.e. non-decision time, drift rate, starting point, and threshold; (Extended fig. 2e)) We found only changing bound is the simplest way to increase both sampling time and performance we monitor when we change airflow (Extended fig. 2f). Here we propose that changing the airflow change the mouse perception of the cost required to perform the task by increasing the threshold.

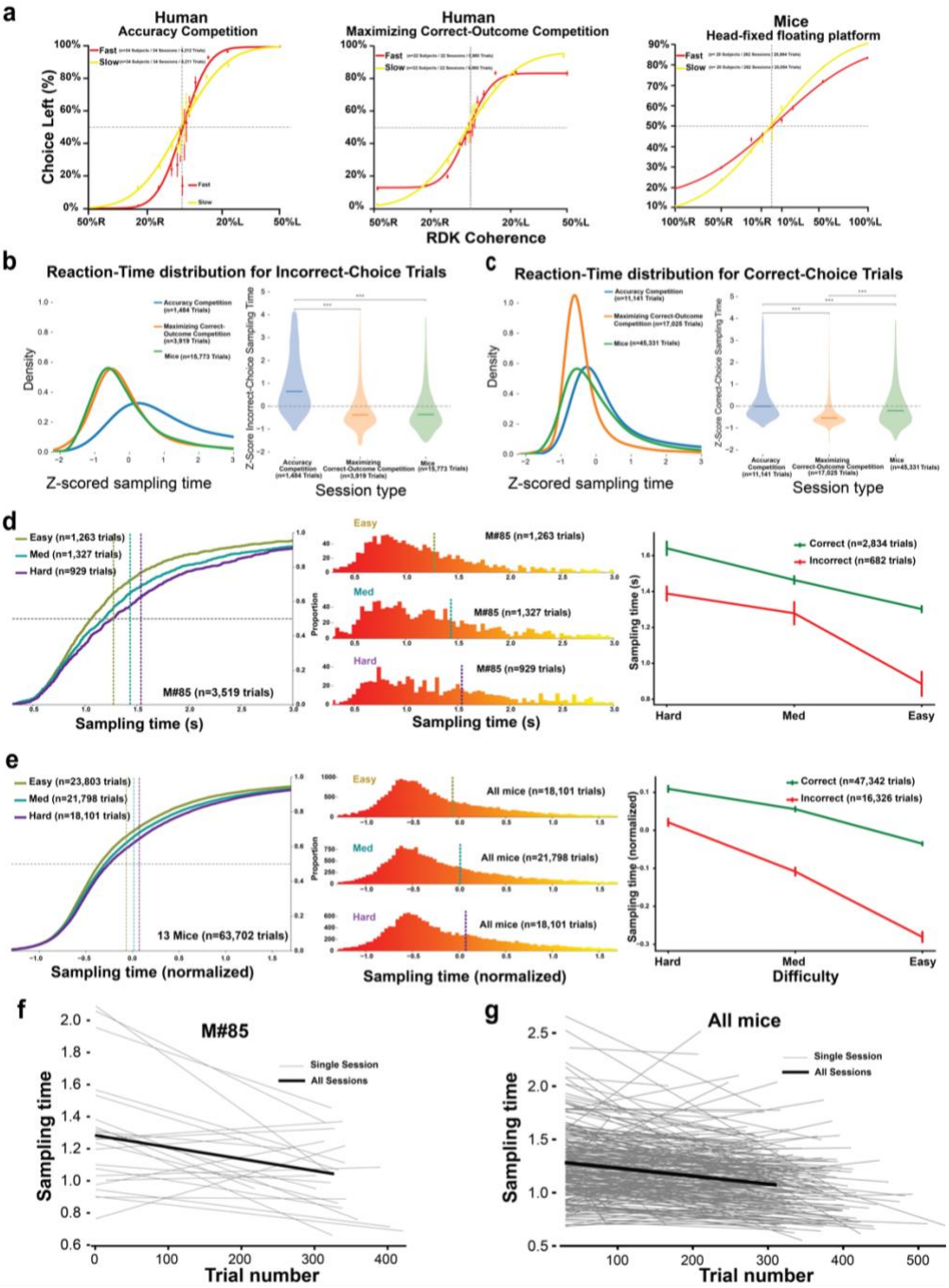

Extended Figure 3. Fast decision is a common strategy during voluntary decision making in human and mice a) Psychometric curves show behavioural performance of RDK task across different sampling epochs of voluntary behaviour: fast (red), and slow (yellow) in humans competing for accuracy (left), humans maximizing the count of correct outcomes (middle), and head-fixed mice in nose-poke floating (right). b) Histogram showing incorrect trials distribution during normalized sampling time in human accuracy competition (blue), human maximizing correct outcome competition (orange), and mice floating platform (green). c) as b for correct trials. d) Cumulative density function for RDK difficulties across sampling time (left), histogram of sampling time across RDK difficulties and mean sampling time for correct (green) and incorrect (red) trials across difficulties in an example mouse (c.f: Fig. 1g-l). e) as d for all mice. f) linear fit for sampling time distribution across the timeline of different single sessions in an example mouse (c.f: Fig. 1g-l). g) as f for all mice.

We noticed that mice errors often come from short sampling time on average in comparison to correct trial (Fig. 1i; Extended Fig. 3d & e). This reflects why fast decisions have lower performance in comparison to slow decisions. As mice were habituated to receive their daily source of water only through the timeline of the behavioural session (≈30 min). We assumed that mice alternate between fast and slow decisions as they aim to collect as much water (reward) during the limited timeline of the behavioural session. In order to understand the psychophysical basis of fast errors in mice, we performed a human experiment, in which subjects were asked to voluntarily sample RDK task to perform 2AFC task in two different contexts. In context 1, subjects were sharing the same computer room while being asked to compete for accuracy. During short breaks, subjects received a ranking based on their accuracy (percent of correct trials; (Extended fig. 3a, left)). In context 2, subjects were asked to compete for maximizing correct trials. In this case subjects used to receive a ranking based on the count of correct trials (number of correct trials; (Extended fig. 3a, middle)). We found head-fixed mice and humans competing for maximum correct trials exhibit the phenomenon of fast (biased) and slow (accurate) decisions (Extended fig. 3b, c). We also check on the distribution of fast and slow decision across the timeline of each session. We found a pattern that sampling time tend to slightly decrease as mice read the end of the session, collecting more reward. We assume that this consistent pattern relates to the dimensioning value of the water drop as mice become sated by the end of the session. Meanwhile, it also shows the mice don't suffer from fatigue along the timeline of session.

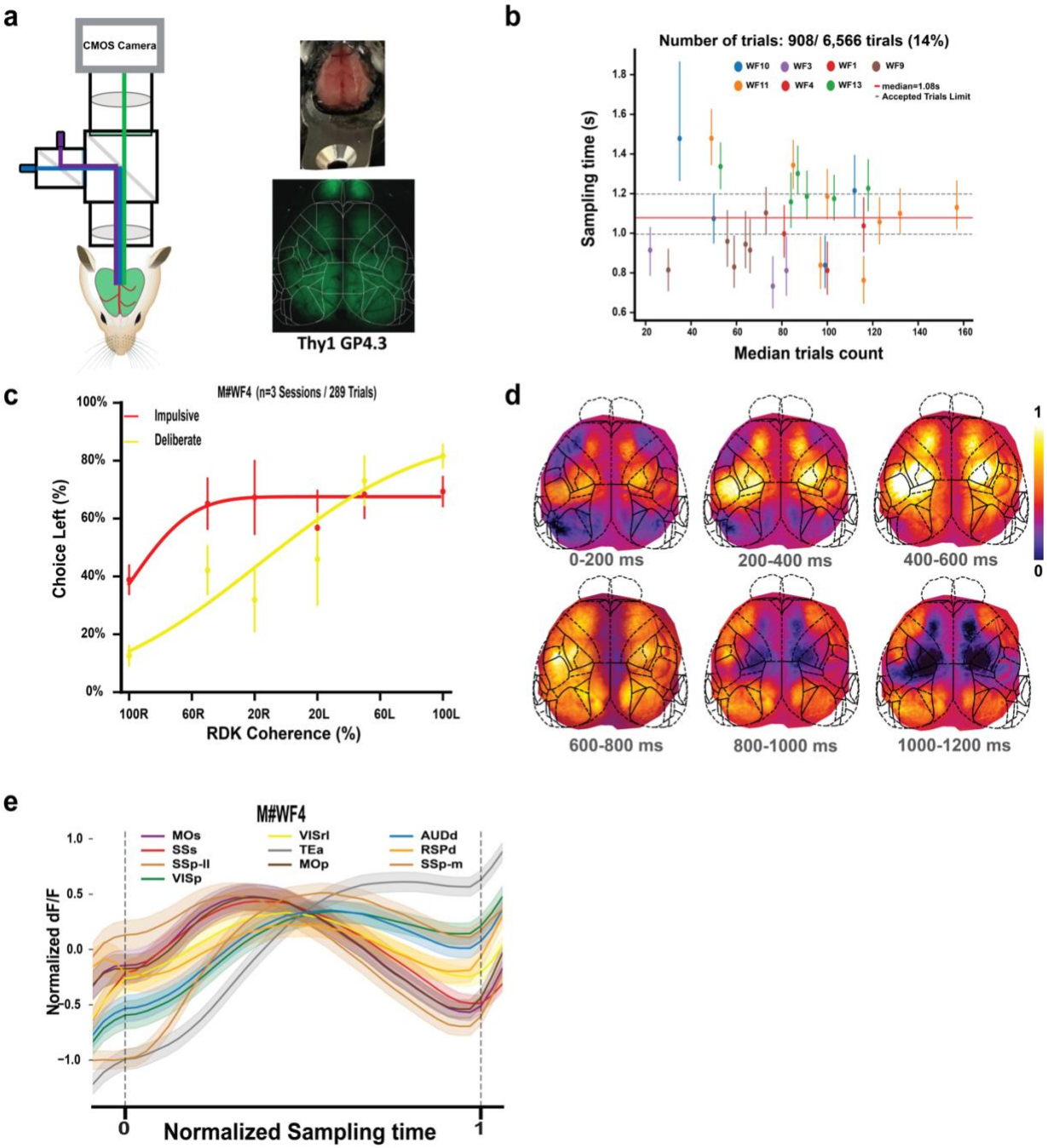

Extended Figure 4. Widefield imaging calcium dynamics during fast and slow behaviour. a) Schematic of widefield imaging system (left), clear skull widefield view under white light (top right) and blue light (bottom right). b) Psychometric curve showing average performance of widefield mice during impulsive and deliberate decisions. b) Temporal range showing select widefield imaging sessions across mice to investigate decision making during sampling time ranging within 1000 to 1200 ms. c) Psychometric curve showing average performance of an example mouse during fast and slow decisions (c.f Fig 2 b, c). d) Pixelwise heat-map from example mouse showing calcium signal propagation across sampling time in typical trails (c.f Fig. 2b). e) Averaged calcium activity during typical trials from different cortical areas for mouse in d across sessions.

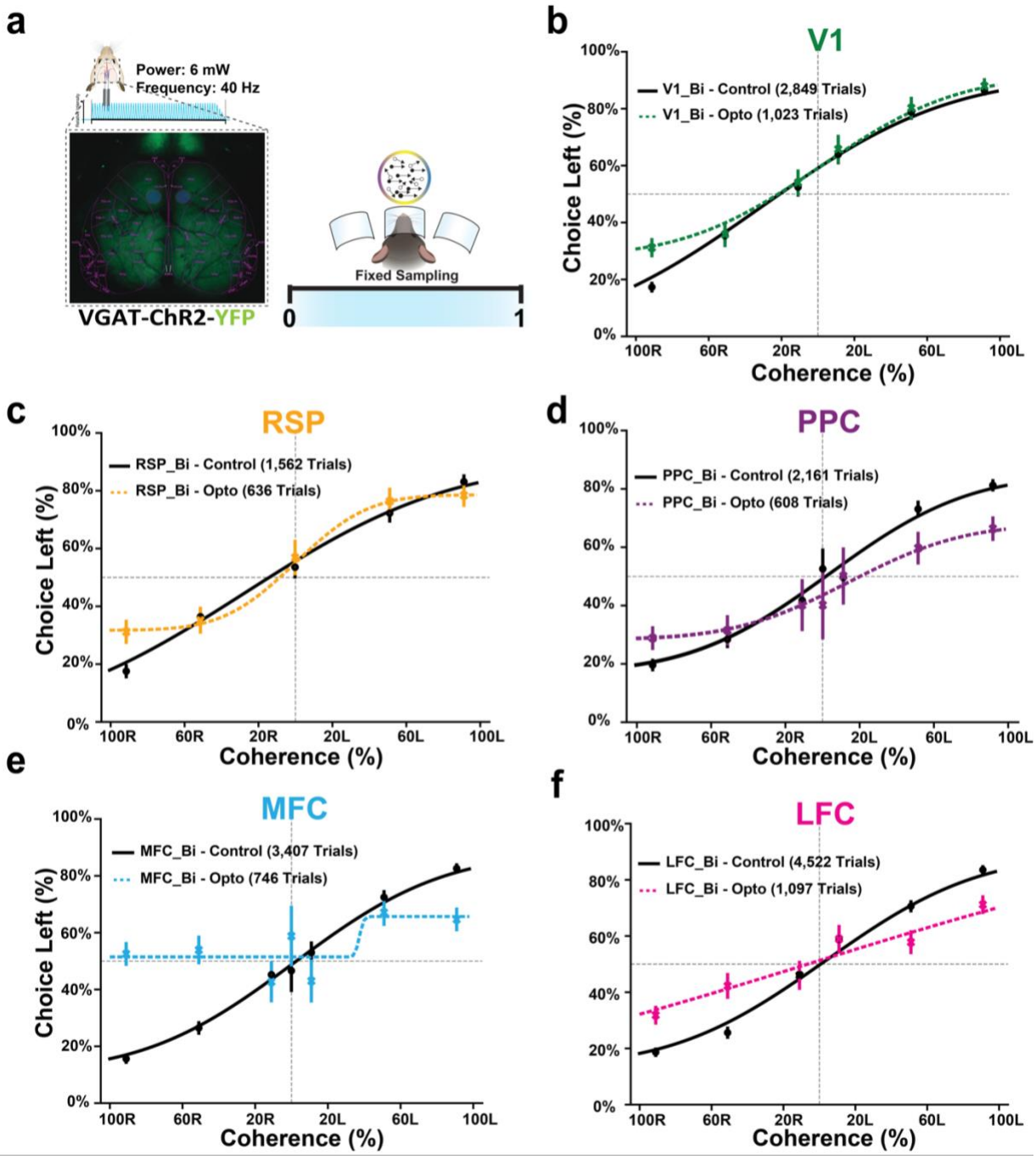

Extended Figure 5. Full optogenetic inhibition of different cortical areas during 1s fixed sampling time in RDK task. a) Schematic showing temporal range of inactivation of different cortical areas. Bilateral fiberoptic targets different cortical areas in a skull cleared vgat-chr2 mice. b-f) Psychometric curve showing mice behavioural performance across control trials (solid line) and optogenetic trials (dashed line) for visual cortex (green), retrosplenial cortex (orange), posterior parietal cortex (violet), medial frontal cortex (blue), and lateral frontal cortex (magenta).

849

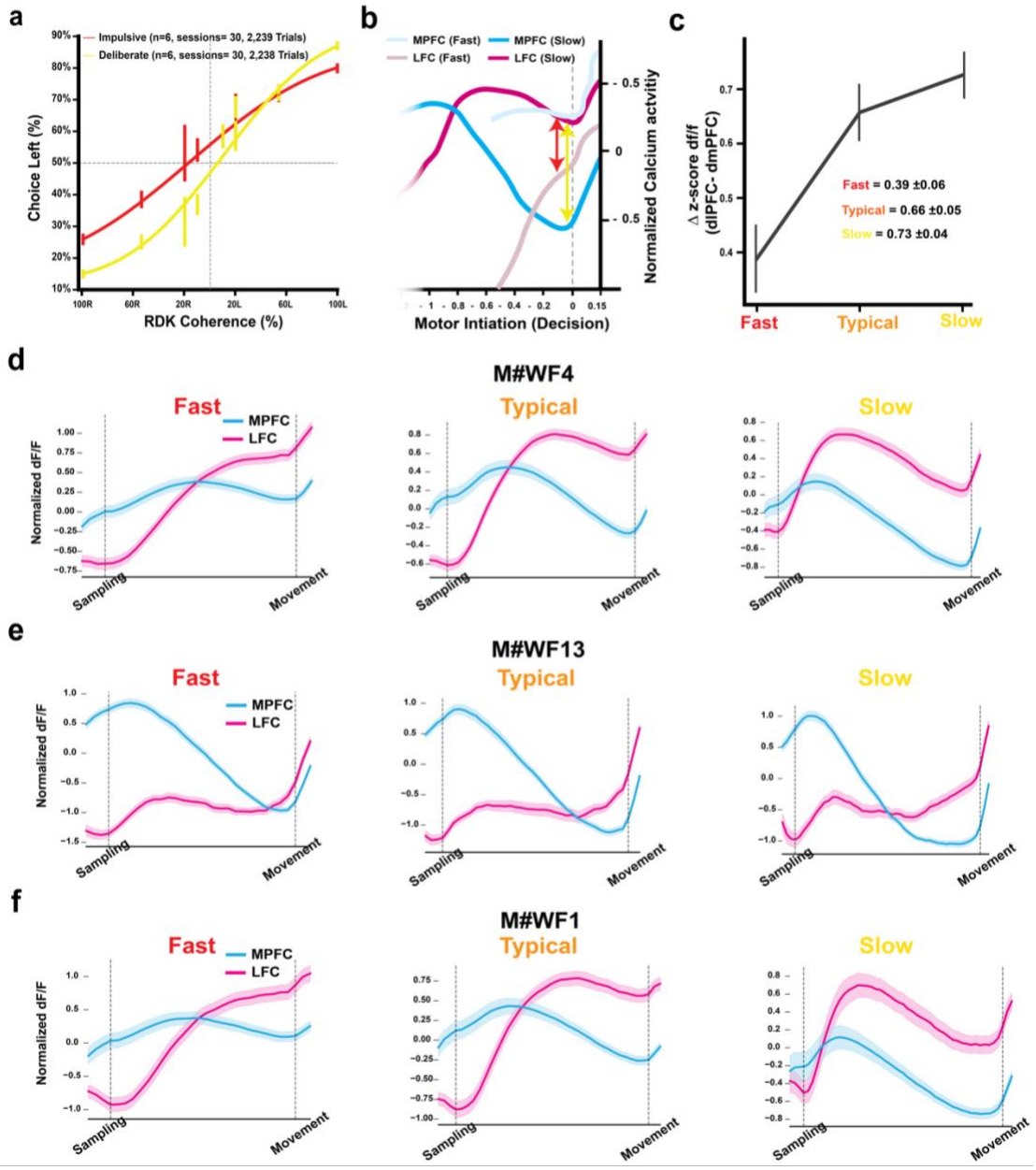

Extended Figure 6. Frontal calcium wave dynamics reflects behavioural strategy. a) Psychometric curve showing fast and slow behavioural signature across widefield mice. b) Example widefield session showing fast behaviour in MFC (faint blue) and LFC (faint magenta) calcium activity, and slow behaviour in MFC (blue) and LFC (magenta) calcium activity binned to motor initiation. Red and yellows arrows point out the difference between fast and slow trials in the calcium activity of MFC and LFC, respectively, at the end of sampling**.** c) Average difference in calcium activity between MFC and LFC at the end of sampling during impulsive, typical and deliberate behavioural strategy across mice (n=6). d-f) Widefield imaging from Medial (blue) and lateral (magenta) at frontal cortex across different strategies are consistent in single behavioural sessions across different mice.

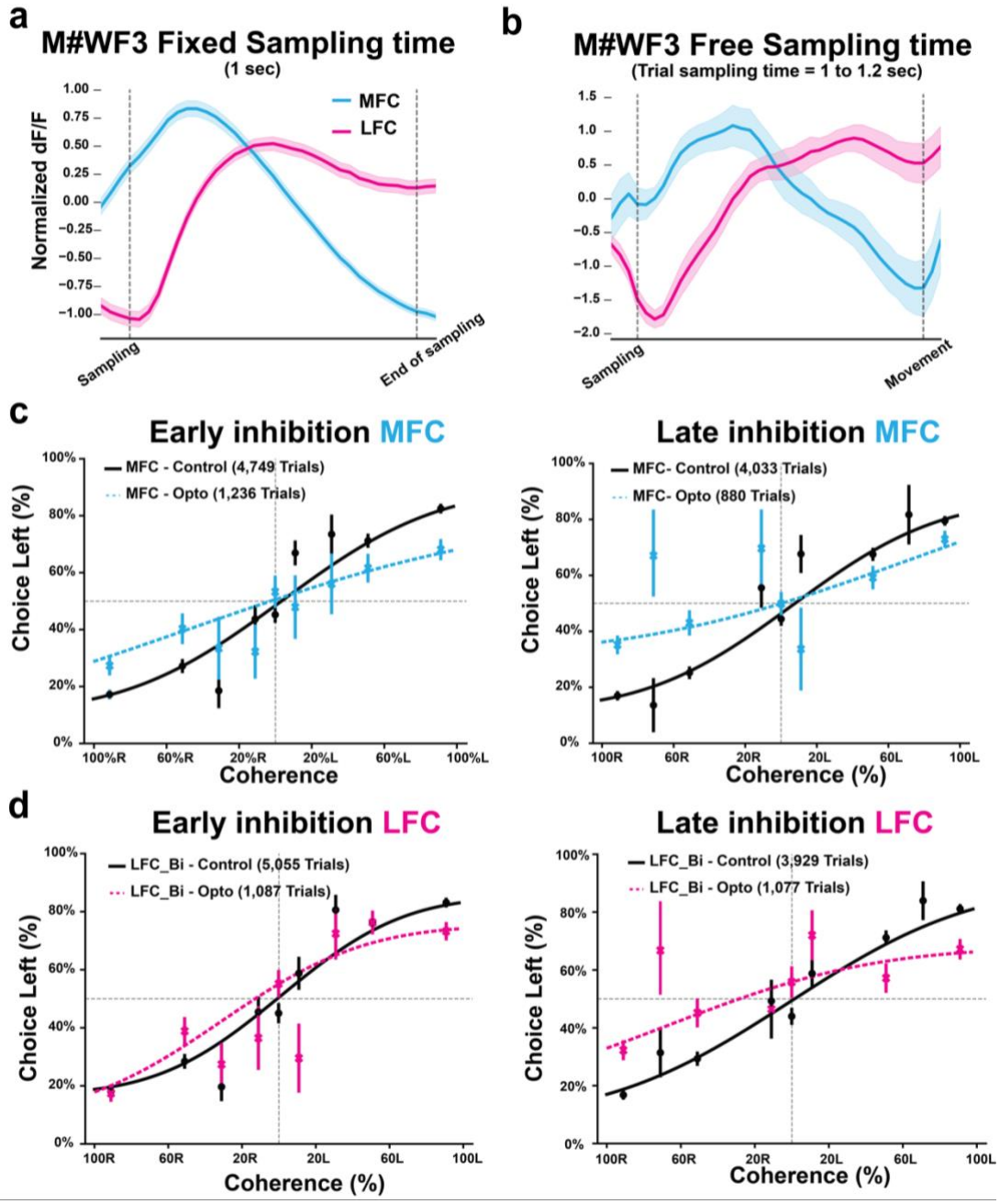

Extended Figure 7. Optogenetic targeting for antipodal frontal calcium wave. a) Frontal calcium wave dynamics during widefield imaging during 1 second fixed sampling time in an example mouse. b) Frontal calcium wave dynamics during typical free sampling time (1-1.2 second) from the same mouse in (a). c-d) Psychometric curve showing mice behavioural across control trials (solid) and optogenetic trials (dashed) for early inhibition (left) and late inhibition (right) in MFC (blue) and LFC (magenta).

853

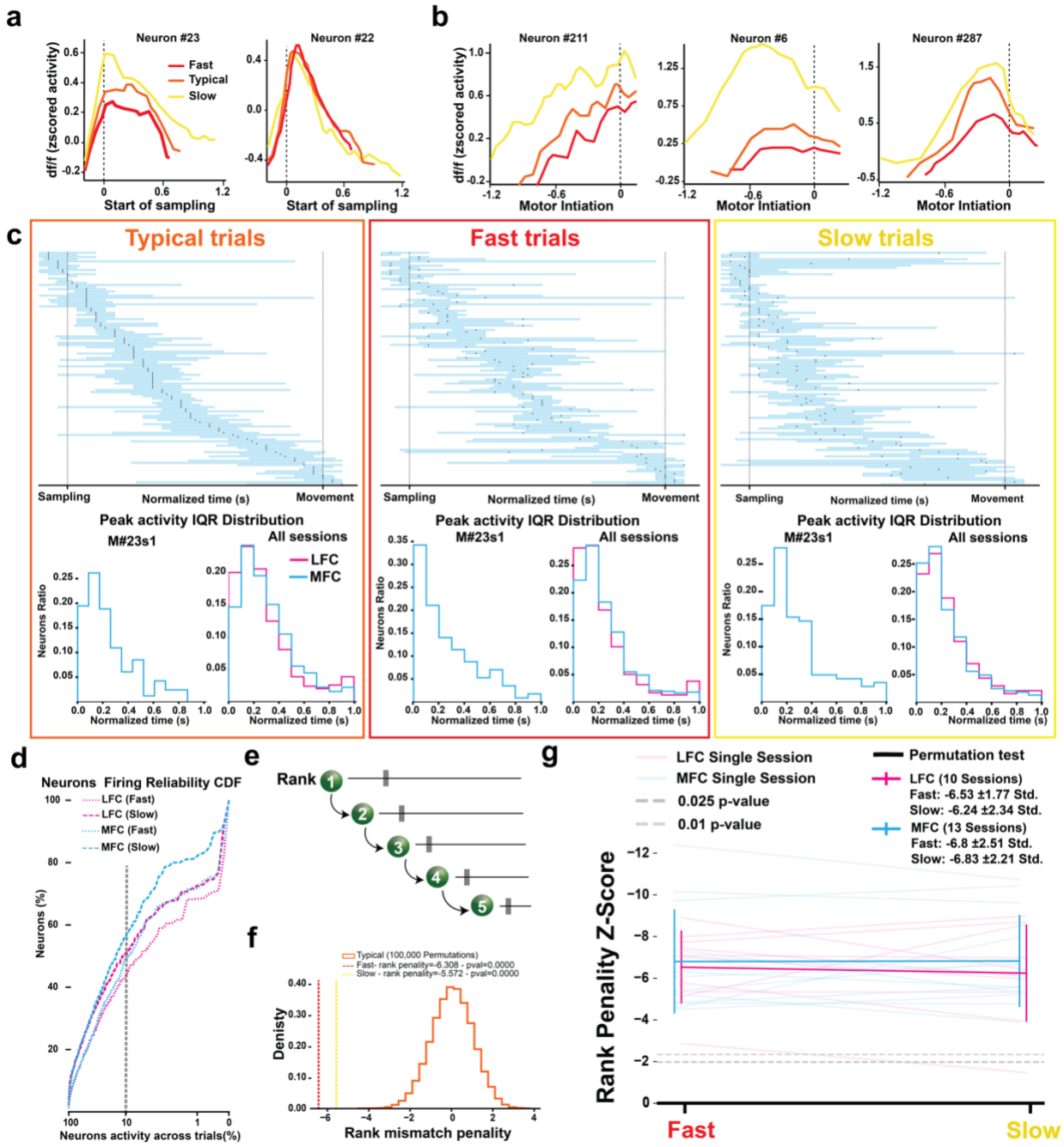

Extended Figure 8. Consistent temporal sequence of l2/3 neurons activation during fast and slow behavioural strategies. a & b) neural activity tuning from example neurons across different behavioural strategies show temporally consistent peak activity. c) Top, IQR for active neurons during sampling time in LFC (magenta) and MFC (blue) across typical trials (orange), fast (red) and slow (yellow) strategies in an example mouse. Bottom left, cumulative density frequency and histogram showing drift in neural peak activity across all trial, impulsive and deliberate in example session. Bottom right, same as middle for all neurons across all sessions in both MFC and LFC. d) Reliability of neuronal firing across trials during fast and slow trials in MFC and LFC. e) Schematic of neural sequences activation with distinct temporal activity order. f) Permutation test for neurons temporal ranking in typical trials of an example session (orange histogram). Fast (red) and slow (yellow) trials rank penalty to typical trials ranking for the same session. g) Ranking neural sequence activation across fast and slow strategy across all sessions in comparison to typical trials shuffled randomly using permutation test.

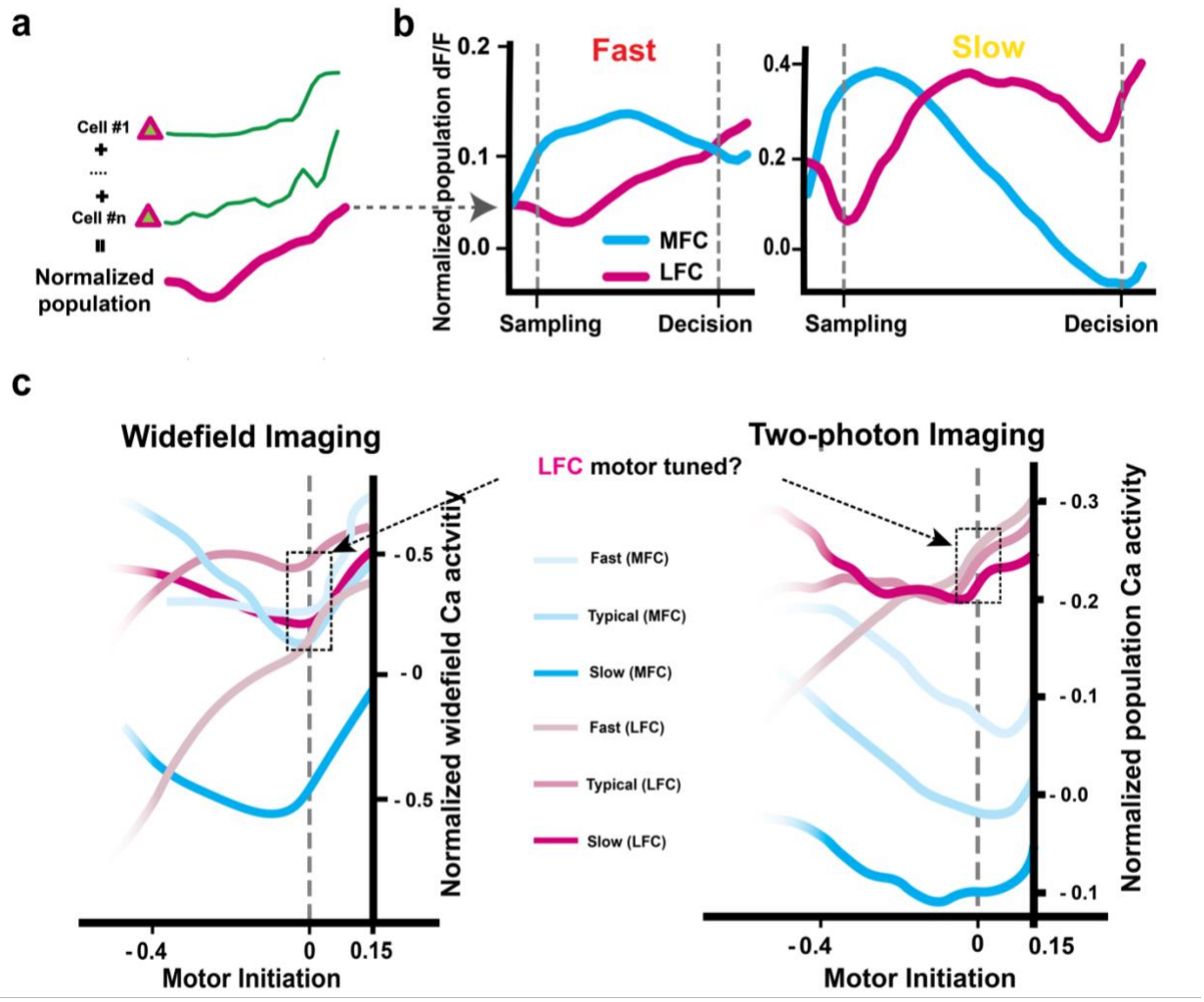

Extended Figure 9. Consistent wave dynamics of l2/3 neurons across fast and slow behavioural strategies in mouse frontal cortex. a) Left, schematic diagram showing the procedure for calculating population responses. B), Population responses for fast (left) and slow (right) behavioural strategies combining MFC (blue) and LFC (magenta). c) Consistent wave dynamics in mouse frontal cortex using widefield imaging (left) and two photon imaging (right).

855

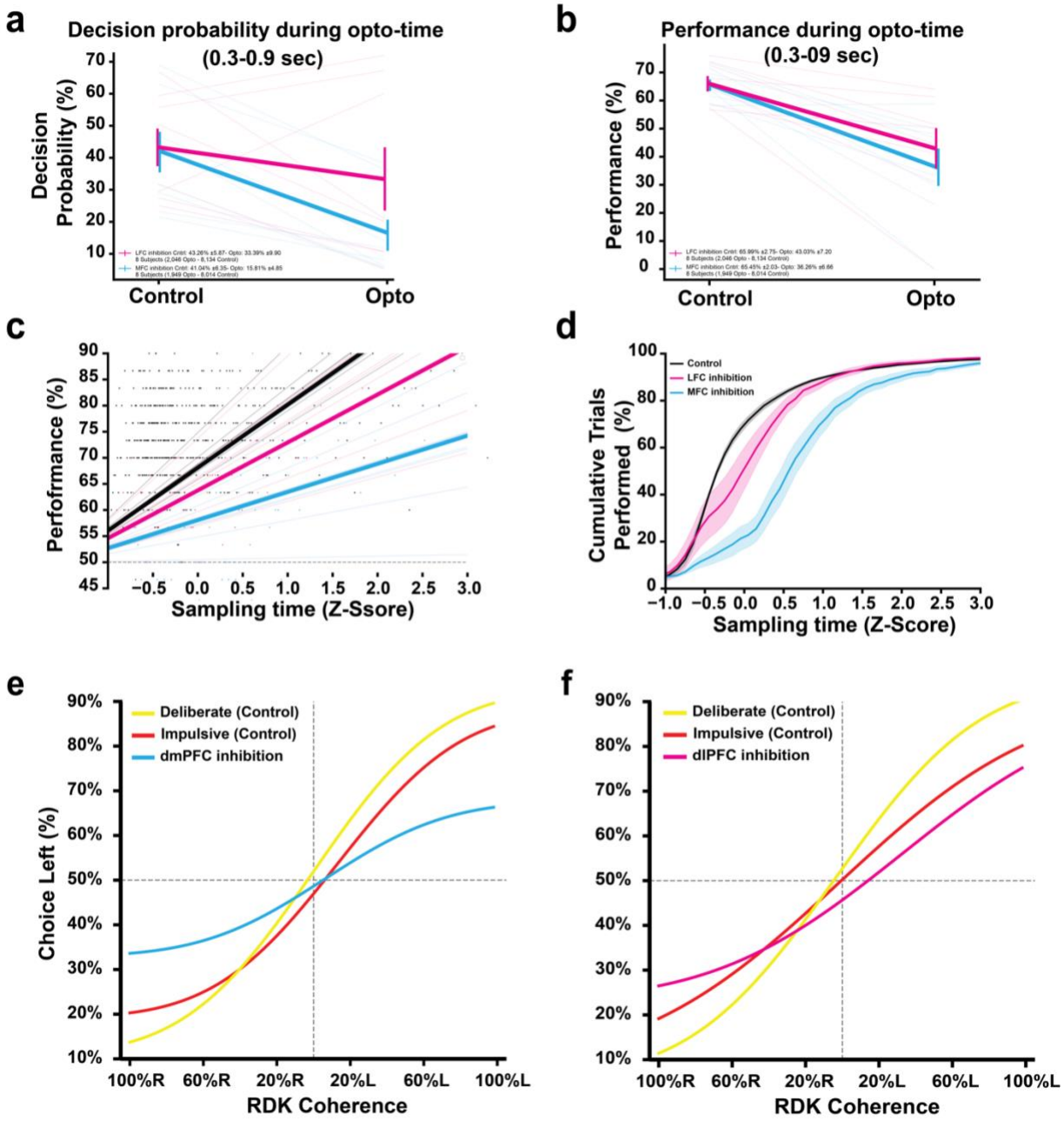

Extended Figure 10. Free sampling optogenetic mid-inhibition of frontal cortical areas in RDK task. a) Early effect of optogenetic inhibition on decision probability (0.3-0.9 sec). b) same as a for decision performance. c) Linear fit of animals' performance during control (black), MFC inhibition (blue) and LFC inhibition (magenta) as a function of z-scored sampling time. d) Cumulative trial distribution during MFC inhibition (blue) and LFC inhibition (magenta) in comparison to control (black) across z-scored sampling time. e-f) Mice behavioural performance across control trials of deliberate, control impulsive and optogenetic trials during free sampling time inhibition of MFC (blue) and LFC (magenta).

856

857

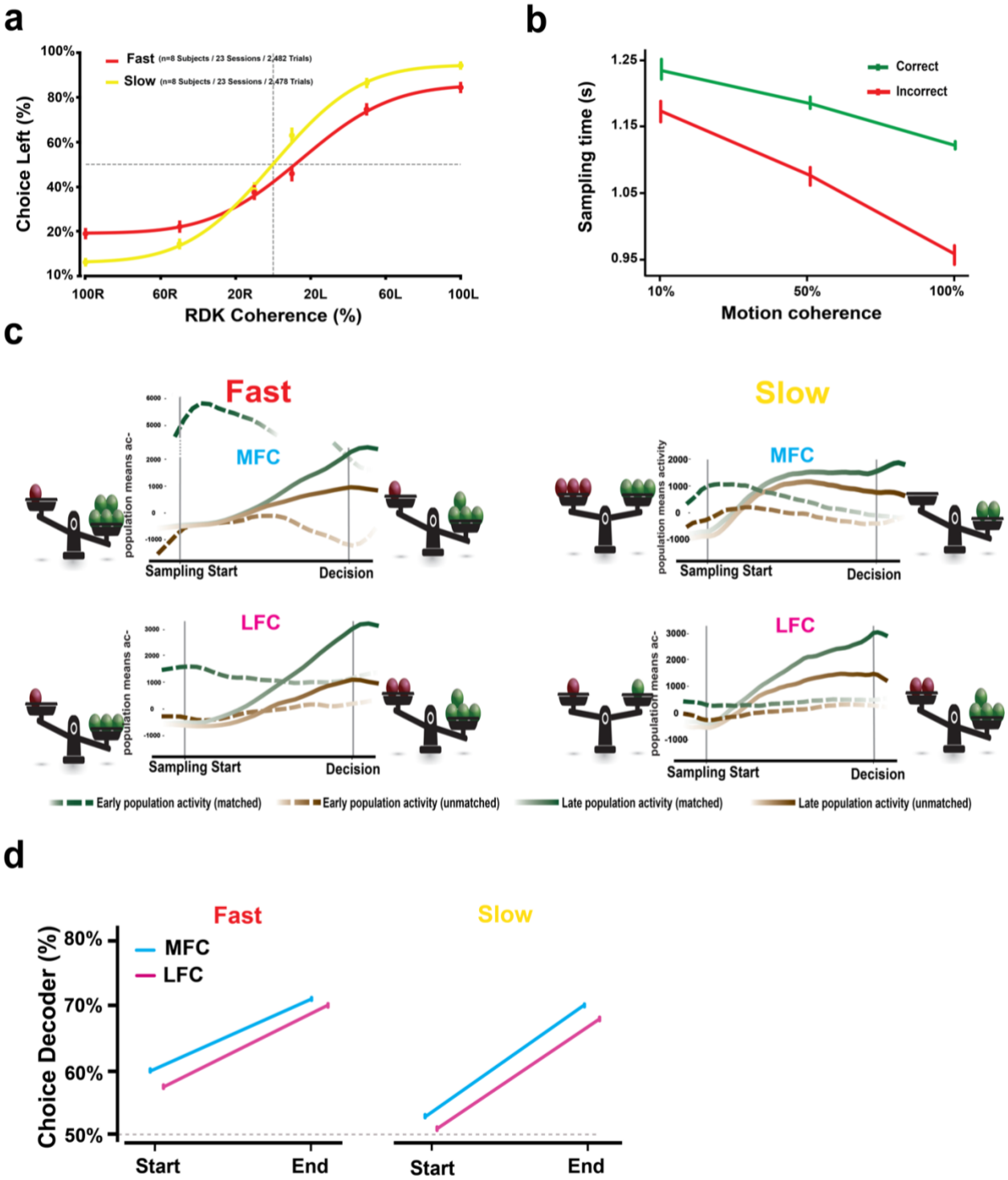

Extended Figure 11. Choice selective neural population sequence encoding choice during fast and slow behavioural strategies. a) Mice under two-photon microscope exhibit classical performance signature during fast and slow strategies. b) Average sampling time distribution across difficulties for correct (green) and incorrect (red) in all mice under two-photon imaging. c) Average population activity at the start of sampling (dashed) and end of sampling (solid) for matching (green) and mismatching (brown) over sampling during fast (left panel) and slow (right panel) in MFC (top) and LFC (bottom). Scales and balls illustrate the ratio of neural responses at the start and end of sampling. d) Choice decoding accuracy at the start of and end sampling during fast and slow behaviour

858

859

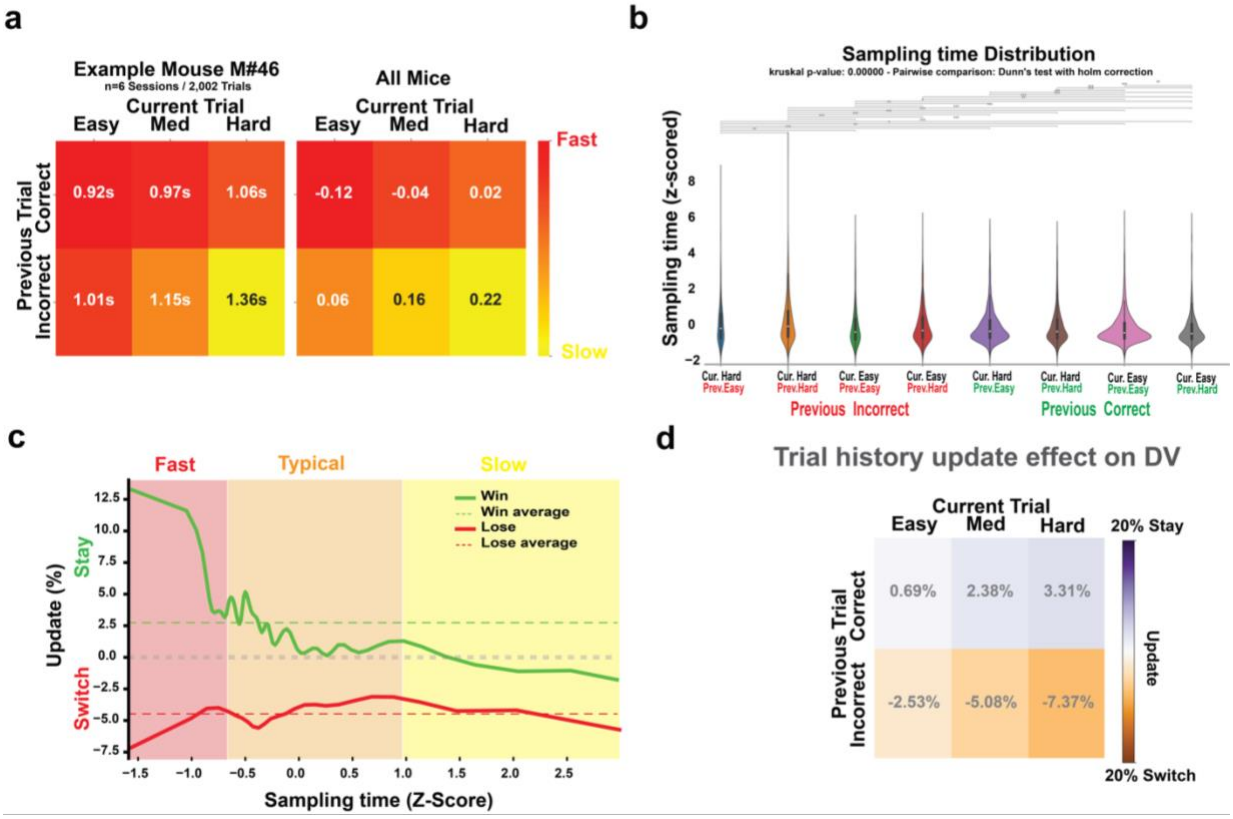

Extended Figure 12. Trial history effect commands fast behavioral strategy. a) Heatmap grid showing sampling time distribution as a function of previous trial outcome and current trial evidence for an example mouse (left) and all mice (right). b) Pairwise comparison showing that previous trial outcome significantly changes sampling time for current trial across difficulties. c) Trajectory of win-stay (green) and lose-switch (red) probabilities across different sampling time. d) Previous trial outcome affects win-stay/lose-switch update relative to current trial difficulty.

860

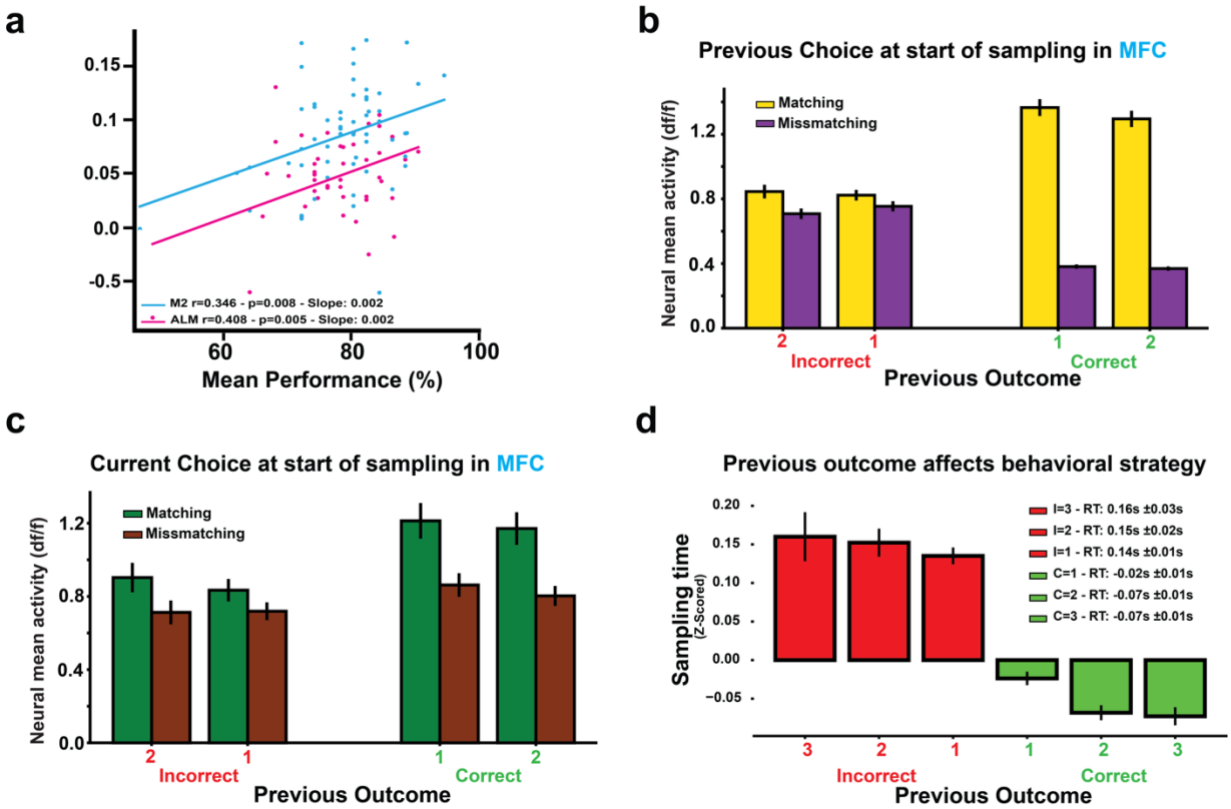

Extended Figure 13. MFC initial activity guides behavioural strategy. a) Population activity in MFC and LEF at the start of sampling corelates with mouse performance. b) Previous trial outcome history modulates the activity of previous choice selective neurons at the start of sampling c) same as b for current choice selective neurons at the start of sampling. d) the sum of previous correct outcomes correlated with a decrease in the sampling time for the next trial, while the sum of previous incorrect outcomes correlated with an increase in sampling time in the following trial.

861

862

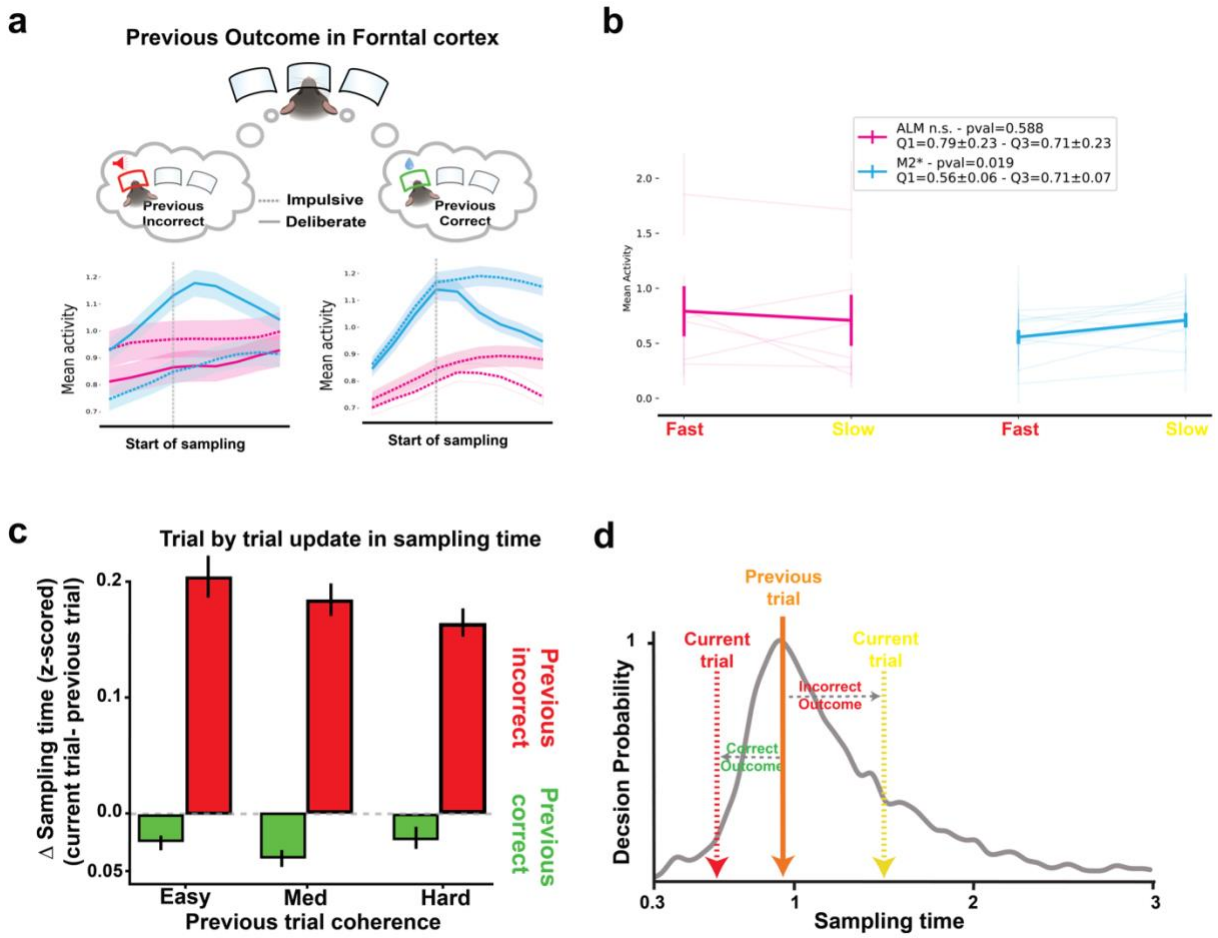

Extended Figure 14. Previous outcome and stimulus difficulty update behavioural strategy. a) Top, schematic showing the effect of previous trial outcome on current trial population activity at the start of sampling. Bottom, average neural activity for neurons significantly tuned for previous trial outcome (incorrect, left panel; correct, right panel) in MFC (blue) and LFC (magenta) during fast (dashed) and slow (solid) strategies. b) MFC previous incorrect choices selective neurons significantly discriminate fast and slow strategies at the start of sampling. c) Shifts in sampling time between previous trial and current trial is dependent on both previous trial evidence and outcome. d) Schematic partially describes the variability of sampling time as function of previous trial outcome.

863

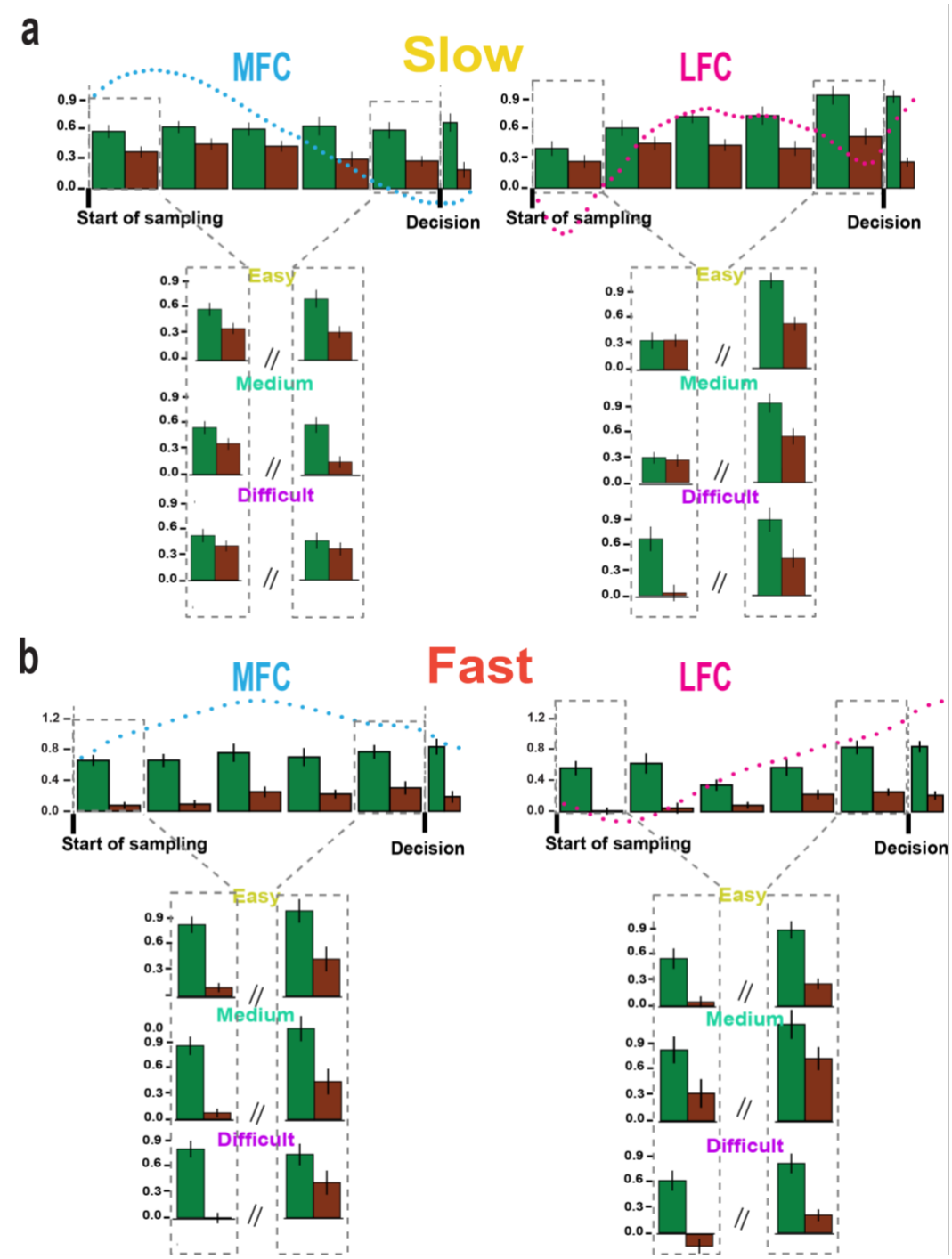

Extended Figure 15. Choice coding efficiency reflects attending to sensory evidence during slow choices. a) Top, Neural responses of sequence choice-selective neurons according to their peak activity for both matched (green) and mismatch trials over sampling during slow behavioural strategy in MFC and LFC. Bottom, difference between matched (green) and mismatch neural activity at the start of sampling and end of sampling across different difficulties in MFC and LFC during slow behavioural strategy. b) as for a for fast behavioural strategy

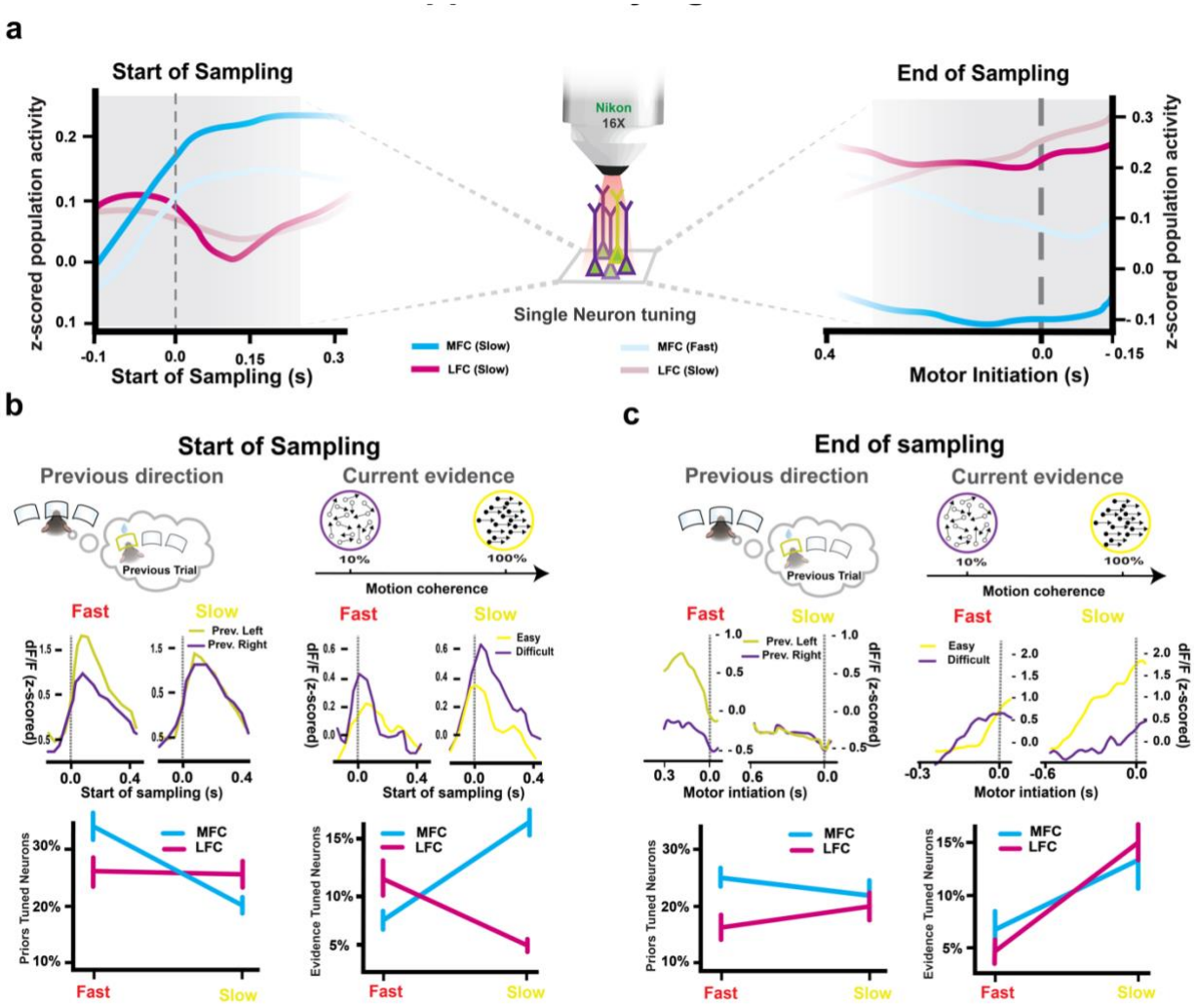

Extended Figure 16. Neural representation of trial history and stimulus evidence during impulsivity and deliberation a) Neural population activity of MFC (blue) and LFC (red) at the start of sampling (left) and end of sampling (right). c) Top, schematic for investigating previous trial choice direction at start of sampling and stimulus evidence at current trial. Middle left, example neurons tuning for pervious trial direction at both impulsive and deliberate trials. Middle right, example neurons tuning for stimulus evidence at both impulsive and deliberate trials. Bottom left, precent of neurons significantly firing for previous trial choice direction at start of sampling during impulsive and deliberate trials in both MFC (blue) and LFC (magenta). Bottom right, precent of neurons significantly firing for stimulus evidence at start of sampling during impulsive and deliberate trials in both MFC (blue) and LFC (magenta). c) as b for impulsive and deliberate trials at the end of sampling.

865

Extended Figure Legends

Extended Figure 1. Novel nose-poke floating-platform approach to study mechanisms of voluntary decision-making in head-fixed mice. a) 3D rendition of sideview (left), top view (middle), and bottom view (right) of nose-poke floating-platform for head-fixed mice performing Random Dots Kinematogram (RDK) task. b) Structure for free sampling RDK task (left), psychometric performance for an example mouse over sessions (middle), and average sampling time across different coherences for right and left choices (right). c) Task structure for fixed variable sampling time in RDK task (left), psychometric performance for an example mouse over sessions (middle), and mouse performance across different difficulties during different fixed variable sampling time (right).

Extended Figure 2. Cost manipulation in nose-poke floating-platform increase sampling time and performance. a) Schematic showing dynamic sampling strategy in mice using nose-poke floating platform involved a range of fast and slow decisions that can be manipulated by changing airflow (cost). b) Changing the cost of making a choice shifts sampling time distribution from a session to another. Sessions with longer sampling time distribution exhibit better performance (c) and adaptive optimal sampling strategy across difficulties (d). e) Top, schematic of drift diffusion model (DDM) and, bottom right, basic elements that controls a DDM based decision making process. f) Changing different parameters of DDM such as drift rate (left) and Boundary (right) with consequent effect on both sampling time and with performance. Out of the four basic DDM parameters, only changes in boundary (threshold) leads to a combined increase in sampling time and performance.

Extended Figure 3. Fast decisions are more common during behavioural strategies aim at maximizing outcome in human and mice a) Psychometric curve show behavioural performance across different sampling epochs: fast (red), and slow (yellow) in humans competing for accuracy (left), maximizing the count of correct outcomes (middle), and mice in nose-poke floating platform performing RDK task. b) Histogram showing incorrect trials distribution during normalized sampling time during human accuracy competition (blue), human maximizing correct outcome competition (orange), and mice floating platform (green). c) as b for correct trials. d) Cumulative density function for RDK difficulties across sampling time (left), histogram of sampling time across RDK difficulties and mean sampling time for correct (green) and incorrect (red) trials across difficulties in an example mouse (c.f: Fig. 1g-l). e) as d for all mice. f) linear fit for sampling time distribution across the timeline of different single sessions in an example mouse (c.f: Fig. 1g-l). g) as f for all mice.

Extended Figure 4. Widefield imaging calcium dynamics during fast and slow behaviour. a) Schematic of widefield imaging system (left), clear skull widefield view

under white light (top right) and blue light (bottom right). b) Psychometric curve showing average performance of widefield mice during impulsive and deliberate decisions. b) Temporal range showing select widefield imaging sessions across mice to investigate decision making during sampling time ranging within 1000 to 1200 ms. c) Psychometric curve showing average performance of an example mouse during fast and slow decisions (c.f Fig 2 b, c). d) Pixelwise heat-map from example mouse showing calcium signal propagation across sampling time in typical trails (c.f Fig. 2b). e) Averaged calcium activity during typical trials from different cortical areas for mouse in d across sessions.

Extended Figure 5. Full optogenetic inhibition of different cortical areas during 1s fixed sampling time in RDK task. a) Schematic showing temporal range of inactivation of different cortical areas. Bilateral fiberoptic targets different cortical areas in a skull cleared vgat-chr2 mice. b-f) Psychometric curve showing mice behavioural performance across control trials (solid line) and optogenetic trials (dashed line) for visual cortex (green), retrosplenial cortex (orange), posterior parietal cortex (violet), medial frontal cortex (blue), and lateral frontal cortex (magenta).

Extended Figure 6. Frontal calcium wave dynamics reflects behavioural strategy. a) Psychometric curve showing fast and slow behavioural signature across widefield mice. b) Example widefield session showing fast behaviour in MFC (faint blue) and LFC (faint magenta) calcium activity, and slow behaviour in MFC (blue) and LFC (magenta) calcium activity binned to motor initiation. Red and yellows arrows point out the difference between fast and slow trials in the calcium activity of MFC and LFC, respectively, at the end of sampling**.** c) Average difference in calcium activity between MFC and LFC at the end of sampling during impulsive, typical and deliberate behavioural strategy across mice (n=6). d-f) Widefield imaging from Medial (blue) and lateral (magenta) at frontal cortex across different strategies are consistent in single behavioural sessions across different mice.

Extended Figure 7. Optogenetic targeting for antipodal frontal calcium wave. a) Frontal calcium wave dynamics during widefield imaging during 1 second fixed sampling time in an example mouse. b) Frontal calcium wave dynamics during typical free sampling time (1-1.2 second) from the same mouse in (a). c-d) Psychometric curve showing mice behavioural across control trials (solid) and optogenetic trials (dashed) for early inhibition (left) and late inhibition (right) in MFC (blue) and LFC (magenta).

Extended Figure 8. Consistent temporal sequence of l2/3 neurons activation during fast and slow behavioural strategies. a & b) neural activity tuning from example neurons across different behavioural strategies show temporally consistent peak activity. c) Top, IQR for active neurons during sampling time in LFC (magenta) and MFC (blue) across typical trials (orange), fast (red) and slow (yellow) strategies in an example mouse. Bottom left, cumulative density frequency and histogram showing drift in neural peak

activity across all trial, impulsive and deliberate in example session. Bottom right, same as middle for all neurons across all sessions in both MFC and LFC. d) Reliability of neuronal firing across trials during fast and slow trials in MFC and LFC. e) Schematic of neural sequences activation with distinct temporal activity order. f) Permutation test for neurons temporal ranking in typical trials of an example session (orange histogram). Fast (red) and slow (yellow) trials rank penalty to typical trials ranking for the same session. g) Ranking neural sequence activation across fast and slow strategy across all sessions in comparison to typical trials shuffled randomly using permutation test.

Extended Figure 9. Consistent wave dynamics of l2/3 neurons across fast and slow behavioural strategies in mouse frontal cortex. a) Left, schematic diagram showing the procedure for calculating population responses. B), Population responses for fast (left) and slow (right) behavioural strategies combining MFC (blue) and LFC (magenta). c) Consistent wave dynamics in mouse frontal cortex using widefield imaging (left) and two photon imaging (right).

Extended Figure 10. Free sampling optogenetic mid-inhibition of frontal cortical areas in RDK task. a) Early effect of optogenetic inhibition on decision probability (0.3-0.9 sec). b) same as a for decision performance. c) Linear fit of animals' performance during control (black), MFC inhibition (blue) and LFC inhibition (magenta) as a function of z-scored sampling time. d) Cumulative trial distribution during MFC inhibition (blue) and LFC inhibition (magenta) in comparison to control (black) across z-scored sampling time. e-f) Mice behavioural performance across control trials of deliberate, control impulsive and optogenetic trials during free sampling time inhibition of MFC (blue) and LFC (magenta).

Extended Figure 11. Choice selective neural population sequence encoding choice during fast and slow behavioural strategies. a) Mice under two-photon microscope exhibit classical performance signature during fast and slow strategies. b) Average sampling time distribution across difficulties for correct (green) and incorrect (red) in all mice under two-photon imaging. c) Average population activity at the start of sampling (dashed) and end of sampling (solid) for matching (green) and mismatching (brown) over sampling during fast (left panel) and slow (right panel) in MFC (top) and LFC (bottom). Scales and balls illustrate the ratio of neural responses at the start and end of sampling. d) Choice decoding accuracy at the start of and end sampling during fast and slow behaviour

Extended Figure 12. Trial history effect commands fast behavioral strategy. a) Heatmap grid showing sampling time distribution as a function of previous trial outcome and current trial evidence for an example mouse (left) and all mice (right). b) Pairwise comparison showing that previous trial outcome significantly changes sampling time for current trial across difficulties. c) Trajectory of win-stay (green) and lose-switch (red)

probabilities across different sampling time. d) Previous trial outcome affects win-stay/lose-switch update relative to current trial difficulty.

Extended Figure 13. MFC initial activity guides behavioural strategy. a) Population activity in MFC and LEF at the start of sampling corelates with mouse performance. b) Previous trial outcome history modulates the activity of previous choice selective neurons at the start of sampling c) same as b for current choice selective neurons at the start of sampling. d) the sum of previous correct outcomes correlated with a decrease in the sampling time for the next trial, while the sum of previous incorrect outcomes correlated with an increase in sampling time in the following trial.

Extended Figure 14. Previous outcome and stimulus difficulty update behavioural strategy. a) Top, schematic showing the effect of previous trial outcome on current trial population activity at the start of sampling. Bottom, average neural activity for neurons significantly tuned for previous trial outcome (incorrect, left panel; correct, right panel) in MFC (blue) and LFC (magenta) during fast (dashed) and slow (solid) strategies. b) MFC previous incorrect choices selective neurons significantly discriminate fast and slow strategies at the start of sampling. c) Shifts in sampling time between previous trial and current trial is dependent on both previous trial evidence and outcome. d) Schematic partially describes the variability of sampling time as function of previous trial outcome.

Extended Figure 15. Choice coding efficiency reflects attending to sensory evidence during slow choices. a) Top, Neural responses of sequence choice-selective neurons according to their peak activity for both matched (green) and mismatch trials over sampling during slow behavioural strategy in MFC and LFC. Bottom, difference between matched (green) and mismatch neural activity at the start of sampling and end of sampling across different difficulties in MFC and LFC during slow behavioural strategy. b) as for a for fast behavioural strategy

Extended Figure 16. Neural representation of trial history and stimulus evidence during impulsivity and deliberation a) Neural population activity of MFC (blue) and LFC (red) at the start of sampling (left) and end of sampling (right). c) Top, schematic for investigating previous trial choice direction at start of sampling and stimulus evidence at current trial. Middle left, example neurons tuning for pervious trial direction at both fast and slow trials. Middle right, example neurons tuning for stimulus evidence at both fast and slow trials. Bottom left, precent of neurons significantly firing for previous trial choice direction at start of sampling during fast and slow trials in both MFC (blue) and LFC (magenta). Bottom right, precent of neurons significantly firing for stimulus evidence at start of sampling during fast and slow trials in both MFC (blue) and LFC (magenta). c) as b for fast and slow trials at the end of sampling.